Texas A&M University
J. Mike Walker'66 Department of Mechanical Engineering
Turbomachinery Laboratory
Tribology Group

LEAKAGE AND DYNAMIC FORCE COEFFICIENTS FOR A STEPPED LABYRINTH SEAL AND A STEPPED POCKET DAMPER SEAL SUPPLIED WITH WET GAS

Annual Progress Report to the TAMU Turbomachinery Research Consortium

TRC-SEAL-01-2021

by

José Torres
Graduate Research Assistant

Luis San Andrés
Mast-Childs Chair Professor
Principal Investigator

Jing Yang
Assistant Research Engineer

June 2021

EXECUTIVE SUMMARY

LEAKAGE AND DYNAMIC FORCE COEFFICIENTS FOR A STEPPED LABYRINTH SEAL AND A STEPPED POCKET DAMPER SEAL SUPPLIED WITH WET GAS

JOSÉ TORRES, LUIS SAN ANDRÉS, AND JING YANG, JUNE 2021

Industrial centrifugal compressors use annular seals, most commonly labyrinth type, to restrict process gas leakage from high-pressure regions to low-pressure regions. Technological developments, particularly in the oil and gas industry, often require centrifugal compressors to operate in harsh environmental conditions. Hence, liquid tolerant compressors enable efficient deep sea oil and gas facilities. Seals supplied with a two-phase flow mixture, liquid in gas (wet gas), can have a large impact on the dynamic stability and leakage performance of oil and gas turbomachinery. Pocket damper seals (PDS) provide a greater amount of effective damping than labyrinth seals (LS).

Using a dedicated wet gas test rig, this report details experimental results for the leakage and dynamic force coefficients for a stepped shaft PDS and a stepped shaft LS with similar geometry and operating conditions. Operating conditions include journal speed up to 5,250 rpm (surface speed = 35 m/s), a pressure ratio (inlet/exit) ranging from 2.5 to 4.2, and an oil in air mixture with a liquid volume fraction up to 10%. The stepped PDS and stepped LS feature the same journal diameter D (127 mm), seal length $L = 0.38D$, and number of blades (4), albeit slightly different clearances. The stepped LS has a clearance that is 15% larger than that of the stepped PDS, thus providing a higher leakage. For operation with pure gas, the seal flow factor ($\bar{\Phi}$) and orifice-like loss coefficient (C_d) are approximately 40% higher for the stepped LS compared to the stepped PDS. The loss coefficient of the stepped PDS decreases as the liquid volume fraction increases, whereas the loss coefficient of the stepped LS increases. For both seals, the real parts of the direct dynamic stiffnesses (corresponding to the direct stiffness coefficients) are nearly identical and insensitive to journal speed, while the cross-coupled stiffnesses are too small for accurate measurement. The stepped PDS produces a significantly higher effective damping coefficient than the stepped LS for all excitation frequencies (10-150 Hz) and three journal speeds (0, 3000, and 5250 rpm). The magnitude of the effective damping coefficient for the stepped PDS tends to grow slightly as the liquid volume fraction increases to 0.7%. Interestingly, broadband subsynchronous vibrations (SSVs) are measured for operation of the stepped PDS with an oil in air mixture. The SSVs do not appear when operating the test rig with the stepped LS.

Table of Contents

Nomenclature

A	Seal Cross-Sectional Area [m^2]
C_e	Idealized Single-Restriction Seal Clearance [m]
C_{eff}	Seal Effective Damping Coefficient, C_{eff} = (Ima(H) – Re(h))/ω [N-s/m]
C_d	Loss Coefficient [-]
C_{ij}	Direct ($i=j$) and Cross-Coupled ($i{\neq}j$) Damping Coefficients [N/m]
$C_{h,ij}$	Direct ($i=j$) and Cross-Coupled ($i{\neq}j$) Damping Coefficients of Support Structure [N/m]
C_r	Seal Radial Clearance [m]
$C_{r,step}$	Seal Radial Clearance at Step Location [m]
d	Seal Cavity/Pocket Depth [m]
D	Journal Diameter [m]
H_{ij}	Direct ($i=j$) and Cross-Coupled ($i{\neq}j$) Complex Stiffnesses [N/m]
H	Arithmetic Average Direct Dynamic Stiffness, $H = (H_{xx} + H_{yy})/2$ [N/m]
h	Arithmetic Average Cross-Coupled Dynamic Stiffness, $h = (H_{xy} - H_{yx})/2$ [N/m]
K_{ij}	Direct ($i=j$) and Cross-Coupled ($i{\neq}j$) Stiffnesses [N/m]
$K_{h,ij}$	Direct ($i=j$) and Cross-Coupled ($i{\neq}j$) Stiffnesses of Support Structure [N/m]
L	Seal Length [m]
$\dot{m}$	Mixture Mass Flow Rate [kg/s]
$\dot{m}_{air}$	Air Mass Flow Rate [kg/s]
$\dot{m}_{oil}$	Oil Mass Flow Rate [kg/s]
M_{sc}	Mass of Seal Stator with Test Seal Installed [kg]
P_s	Mixture Supply Pressure [Pa]
P_e	Mixture Discharge (Exit) Pressure [Pa]
Q_{air}	Air Volumetric Flow Rate [m^3/s]
Q_{oil}	Oil Volumetric Flow Rate [m^3/s]
R	Journal Radius [m]
R_G	Specific Gas Constant of Dry Air [J/(kg-K)]
T_s	Mixture Supply Temperature [K]
u	Journal Surface Speed [m/s]
V_c	Mixture Circumferential Velocity [m/s]

V_e	Mixture Axial Exit Velocity [m/s]
μ_{air}	Air Viscosity [cP]
μ_{oil}	Oil Viscosity [cP]
ρ_{oil}	Oil Density [kg/m³]
ρ_{air}	Average Air Density [kg/m³]
ρ_m	Mixture Density [kg/m³]
$\bar{\phi}$	Modified Flow Factor [(kg-K$^{1/2}$)/(m-s-MPa)]
ω	Excitation Frequency [rad/s]
Ω	Journal Speed [rad/s]

Vectors and Matrices

D	Recorded Seal Stator Displacement
A	Recorded Seal Stator Acceleration
F	Dynamic Load Applied to Seal Stator
$\mathbf{\bar{D}}$	Discrete Fourier Transform of **D**
$\mathbf{\bar{A}}$	Discrete Fourier Transform of **A**
$\mathbf{\bar{F}}$	Discrete Fourier Transform of **F**
H	Complex Dynamic Stiffness Matrix

Abbreviations

FPPDS	Fully Partitioned Pocket Damper Seal
GVF	Mixture Gas Volume Fraction
GMF	Mixture Gas Mass Fraction
HPC	High Pressure Compressor
LMF	Mixture Liquid Mass Fraction, LMF = (1 – GMF)
LPC	Low Pressure Compressor
LS	Labyrinth Seal
LVF	Mixture Liquid Volume Fraction, LVF = (1 – GVF)
PDS	Pocket Damper Seal
SSV	Subsynchronous Vibration
TOR	Tooth-On-Rotor
TOS	Tooth-On-Stator

Introduction

Centrifugal compressors utilize annular gas seals to reduce excessive leakage of the working fluid from high pressure regions to low-pressure regions. Examples of such seals include interstage seals, impeller eye seals, and balance-piston seals [1]. The pocket damper seal (PDS) is a type of gas seal that arose from slight modifications to the conventional labyrinth seal [2]. Unlike a labyrinth seal (LS), which consists of circumferential blades that create 360° cavities, a PDS includes partition walls that divide each cavity into separate "pockets". Figure 1 shows a conventional LS and a PDS featuring its unique partition walls.
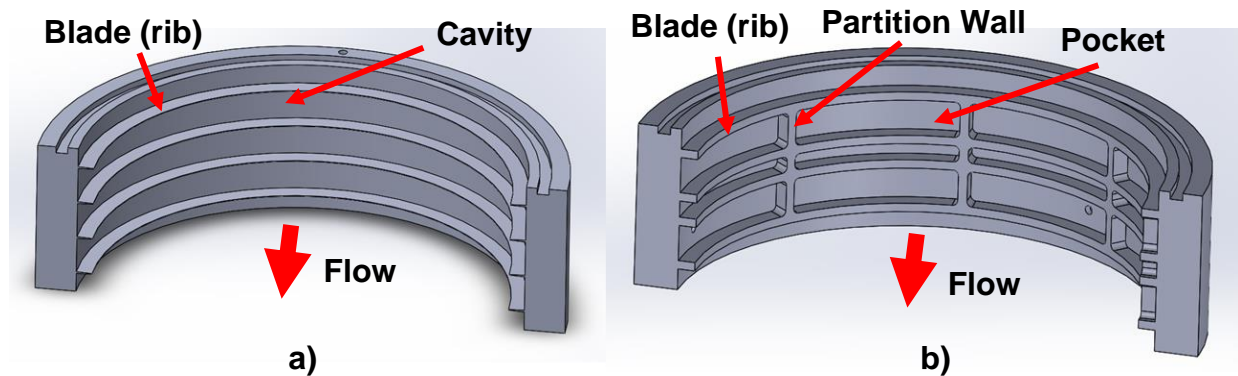
Fig. 1: Illustrations of (a) Labyrinth Seal (LS) and (b) Fully Partitioned Pocket Damper Seal (PDS).

Designers have successfully used PDSs to replace LSs in order to remedy rotordynamic stability issues as PDSs have the ability to increase damping and reduce cross-coupled stiffness [1]. Further technological developments, particularly in the oil and gas industry, call for liquid tolerant centrifugal compressors. The presence of liquid in a gas seal, even if in miniscule amounts, can have a large impact on the rotordynamic stability and leakage characteristics of turbomachinery [3]. Characterizing the dynamic stability and leakage properties of a PDS under wet gas conditions, and benchmarking against a similarly dimensioned LS, will help turbomachinery design engineers in selecting a seal type that best meets their system requirements.

This report charts experimentally derived dynamic force coefficients and leakage for a stepped PDS and a stepped LS installed in a two-phase flow (wet gas) seal test rig. Both the stepped PDS and stepped LS have the same physical dimensions, although differing in clearance due to a manufacturing error.

6

Literature Review

Annular seals in turbomachinery are designed to restrict process gas leakage between a rotor and stator. There exists a variety of seals to choose from when designing turbomachinery, including (but not limited to) labyrinth seals (LS), honeycomb seals, abradable seals, brush seals, and pocket damper seals (PDS). A LS, such as the one depicted in Fig.1, can be constructed as different configurations. A tooth-on-rotor (TOR) LS consists of a seal in which the blades are attached to the spinning rotor. On the other hand, a tooth-on-stator (TOS) LS has its blades attached to the stationary housing. Figure 1 shows a LS with a TOS design. An interlocking LS is a combination of both TOR and TOS configurations.

Labyrinth seals (LS) are often found to cause rotordynamic stability issues in compressors and turbines [1]. Prior experimentation shows that cross-coupled stiffness effects may be significant in LSs, and may in fact lead to rotordynamic instability [1]. These cross-coupled effects are in large part due to the development of a large circumferential velocity of the gas within the cavities [1]. Therefore, seals experiencing a higher degree of pre-rotated flow may have an increased susceptibility to instability issues. A design engineer may implement various modifications to remedy rotordynamic instability issues including the addition of swirl brakes, shunt holes, or replacing the seal with an improved design.

Turbomachinery designers have successfully implemented a PDS design to remedy many instability problems found in centrifugal compressors [1]. In 1993, Vance and Schultz [2] invented the TAMSEAL®, a first PDS derived from a straight through clearance LS. The TAMSEAL® differs from the typical LS with two unique features. First, the seal clearance diverges along the axial flow path. In the TAMSEAL®, the clearance at the seal exit blade is twice as large as the clearance at the upstream inlet blade. The second feature is the introduction of partition walls along the circumferential direction, effectively dividing the cavity into four identical pockets. Prior testing in Ref. [3] shows the TAMSEAL® successfully reduces rotor vibrations, while crossing a critical speed, by as much as 50% when compared to the effect of a similarly dimensioned conventional LS. In addition, the TAMSEAL® successfully decreases the overall synchronous response to an imbalance for operation with supply pressure up to 3.4 bar and rotor speed up to 6000 rpm (surface speed = 32 m/s). Rap tests performed by Vance and Li [4] show the novel seal design dissipates motion much quicker, indicating a much higher effective damping.

In 1995, Richards et al. [5] present two cases in which a PDS successfully solved instability issues in centrifugal compressors, illustrating the usefulness of using PDSs in industrial turbomachinery. The first case study involves three identical trains of back-to-back low-pressure compressors (LPC) and high-pressure compressors (HPC). The authors note that although the rated operating speed of the compressors was 11,000 rpm, the LPC could only achieve 7,500 rpm, whereas the HPC could only achieve 10,600 rpm due to excessive subsynchronous vibrations (SSV) at the center LS. The LPC and HPC experienced SSVs at a frequency equal to the first natural frequency of their respective rotors. The authors believe the initial design analysis severely underestimated the magnitude of the cross-coupled stiffness contribution of the center LS. The operators initially intended to replace the center LS with a honeycomb seal to improve vibration damping, alas were unable due to the long manufacturing lead time. Instead, the operators implemented a PDS with pocket depths specifically designed to optimize damping at the rotor natural frequency. The new configuration completely eliminated the SSV [5].

The second case study in Ref. [5] involves a set of four six-stage compressors in an offshore platform in the North Sea. These compressors were rendered inoperable due to an excessive synchronous vibration. The authors describe severe LS rubs at the center balance piston occurring on multiple occasions. Due to the susceptibility to rubbing and wear, the operators designed a replacement PDS made from polyamide-imide copolymer. The choice of material is based on chemical compatibility with the service conditions and excellent wear properties to prevent damage to the rotor. The results show the PDS reducing SSV amplitudes by as much as 50% at an operating speed of 11,000 rpm, while the improved material allows for operation at tighter clearances due to the reduced concern of damage occurring during a transient seal rubbing event [5].

In 1999, Ransom et al. [6] present additional early experimentation regarding the performance of PDSs. The authors corroborate the results of Vance and Li [4] by identifying the rotordynamic force coefficients of a LS before and after adding radial baffles, effectively changing the configuration to that of a PDS. Their results show the presence of radial baffles change the direct damping coefficients from negative to positive while also reversing the direct stiffness from positive to negative. The large direct damping coefficients are significant enough to have a noticeable effect on the logarithmic decrement of the system.

A variety of computational programs exist to predict the rotordynamic performance of PDSs. In 1999, Li and San Andrés [7] develop a single control volume bulk-flow analysis to predict the flow field and force coefficients of a multiple-pocket PDS. The authors compare the analysis to the experimental results obtained by Ransom et al. [6] for a two-blade, four-pocket PDS constructed by adding radial baffles into the cavities of a conventional LS. The model correctly predicts the sign of the direct stiffness (negative) and damping (positive) coefficients, although slightly overestimating the magnitude of damping while underestimating the magnitude of direct stiffness. The bulk-flow model also shows promising results in estimating the sign and magnitude of cross-coupled effects, with the exception of outliers in the experimental data. In 2000, Li et al. [8] use the same bulk-flow analysis to predict the performance of a multiple-blade PDS and provide a comparison to further experimental data. The results show an insensitivity of the force coefficients to rotor speed, while providing excellent correlation between the predicted force coefficients and the experimental force coefficients.

In 2000, Li et al. [9] present early experimental results comparing the performance of a PDS against that of a honeycomb seal. The authors investigate the effect of inlet pre-swirl and seal eccentricity on the performance of both seals. Both seals feature identical diameter, length, and radial clearance. The results indicate the honeycomb seal has a higher effective damping than the PDS. However, the honeycomb seal produces a large positive direct stiffness that would have to be accounted for if replacing a LS. In contrast to these results, the PDS shows a negative direct stiffness (similar to a LS), indicating that the rotor critical speed may not be greatly affected if replacing a LS with a PDS. Thus, the PDS is more suitable to serve as a drop-in-replacement for a conventional LS [9].

A conventional PDS may have inactive cavities between partitioned cavities (pockets). An inactive cavity is one without partition walls, thus cannot block the development of circumferential flow. In 2002, Li et al. [10] investigate the effects of having a fully partitioned PDS (FPPDS) with slots machined into the blades, thus allowing for a small amount of unobstructed axial flow. Measurements of an imbalance response illustrate the effectiveness of the slotted FPPDS in reducing vibration amplitude when compared to a conventional PDS with inactive cavities. In addition, the authors successfully show the slotted FPPDS raises the rotor critical speed, indicating a positive effective stiffness [10].

A need to characterize the performance of a PDS under operating conditions that exist in high-pressure industrial centrifugal compressors prompted Ertas and Vance [11] (2006) to use a modified high-pressure test rig originally intended for use with hydrostatic bearings. The test facility can support rotor speeds up to 20,200 rpm and seals operating with a supply pressure up to 68.9 bar. The authors illustrate the effects of clearance ratio, rotor speed, and excitation frequency on the rotordynamic force coefficients of a 12-blade test PDS and an 8-blade test PDS. While rotor speed has a negligible effect on direct damping, clearance ratio and excitation frequency create a noticeable difference. The authors show an increasing clearance ratio, defined as the ratio between inlet clearance to exit clearance, creates significantly greater direct damping coefficients. The 12-blade test PDS has a clearance ratio of 1:2, while the 8-blade test PDS has a clearance ratio of 1:1.5. Additionally, the results illustrate that the direct damping decreases with excitation frequency; different from the behavior exhibited by most honeycomb seals and hole-pattern seals [11].

In addition to rotordynamic stability, leakage is most important when selecting gas seals for use in turbomachinery. In 2011, Sheng et al. [12] compare the leakage of a LS, a FPPDS, and a honeycomb seal. The three seal types have an inner diameter of 170 mm and a radial clearance of 0.29 mm. The authors estimate an effective clearance as a way to normalize the performance of each seal with respect to the properties of the process fluid and the geometry of the seal entrance. For an inlet pressure up to 20 bar and pressure ratio (inlet/exit) ranging from 1 to 2, the authors find the honeycomb seal consistently leaks the least. The honeycomb seal provides a reduction in effective clearance of about 4% in comparison to that of the LS. On the other hand, the PDS provides an increase in effective clearance of up to 21% at the lowest inlet pressure. Thus, turbomachinery designers should be aware of the higher leakage of a PDS when deciding to incorporate one into their design.

Technological developments and the depletion of oil and gas fields call for centrifugal compressor systems to operate in harsh environmental conditions [3]. In subsea and offshore applications, liquid ingestion into gas centrifugal compressors may be a common occurrence. In 2014, Vannini et al. [3] conduct an in-depth investigation into the rotordynamic effects of wet gas ingestion into a single stage centrifugal compressor. The authors show the centrifugal compressor is able to withstand large amounts of liquid phase, noting that the synchronous vibration level only

exhibits slight increases and the critical speed position is not affected. However, at high flow rate and high liquid to gas density ratios, an unexpected SSV occurs. The SSV appears at a frequency equal to 45% of shaft speed with an amplitude of nearly twice the amplitude of synchronous vibration. A thorough investigation reveals the SSV is closely related to the pressure drop across the balance piston seal, leading the authors to believe the likely cause is liquid accumulation in the LS cavities. Replacing the LS with a FPPDS causes a near complete elimination of the SSV. In the same year, in an effort the better understand this self-exciting phenomenon, Vannini et al. [13] perform an extensive CFD analysis of a LS and PDS operating under a wet gas condition. The analysis corroborates their earlier experimental observations, illustrating that a TOS LS is particularly susceptible to liquid entrapment within the cavities. The authors assert the rotordynamic issues of the LS design are a result of the liquid circulating with significant circumferential momentum within the cavities.

In 2019, San Andrés et al. [14] perform a CFD analysis to determine the leakage, power loss, and force coefficients of a smooth surface annular seal operating with wet gas. The authors report a significant hardening effect in which the direct stiffness of a pure liquid flow turns from negative to positive when the gas volume fraction (GVF) increases to 40%. The authors attribute the stiffening to the drastic reduction in sound speed caused by the presence of a small amount of gas in the mixture, hence creating a more compressible fluid [14]. The CFD model also predicts the effective damping of the seal to increase with a lower GVF; an effect likely caused by a more substantial increase in direct damping rather than the slight increase in cross-coupled stiffness. The CFD analysis illustrates the significant impact that liquid content has on the rotordynamic performance of a gas seal.

In 2020, Delgado et al. [15] present more recent experimentally derived rotordynamic force coefficients for a FPPDS operating with similar speed and pressure as those in industrial multiple-stage compressors, namely a supply pressure of 70 bar(a) and shaft speed equal to 10, 15, and 20 krpm (surface speed = 60, 90, and 120 m/s). The authors demonstrate that the FPPDS direct stiffness tends to decrease as the pressure ratio (exit/inlet) increases. In addition, the experimental results agree with those presented in the paper by Li et al. [9], showing that at low frequencies the FPPDS direct stiffness coefficients are negative and very small. The effective damping coefficient increases with an increase in shaft speed and a reduction in inlet pre-swirl flow. The results indicate

that cross-coupled stiffness is independent of the excitation frequency, and with magnitude increasing with both shaft speed and inlet pre-swirl [15]. The authors also report the FPPDS leaks 20%-25% more than a similarly dimensioned honeycomb seal, thus corroborating prior experimental efforts [12].

In 2020, Cangioli et al. [16] provide a more recent two-control volume bulk-flow model to account for circumferential flow within the pockets. The model includes the equations of flow continuity, circumferential and axial momentum transport, and thermal energy transport. The authors compare their predictions against experimental data gathered for an eight-cavity FPPDS with eight pockets per cavity [17]. The results are very promising, indicating excellent prediction of direct stiffness, cross-coupled stiffness, direct damping, and effective damping for shaft speeds of up to 10,000 rpm (surface speed = 115 m/s) and operation at a maximum pressure ratio (inlet/exit) of two.

In 2021, Yang et al. [18] introduce a simple analytical two-phase flow model to predict the cavity pressures and leakage of both PDSs and LSs operating with a liquid in gas mixture. The novel method adapts the well-known Neumann's Equation to a two-phase flow and uses the properties of an assumed homogenous mixture. The predictions gathered from this simple tool are compared to experimental results for a four-blade, eight-pocket PDS operating with a low pressure drop and at a low speed, and an eight-blade, sixteen-pocket PDS operating with a high pressure drop and at a high speed. For the four-blade PDS, the gas leakage predictions agree quite well with the experimental results, and with cavity pressures deviating from a CFD analysis by no more than 18%. For the eight-blade PDS, predictions for a 92% GVF mixture differ from CFD predictions by at most 6%. Besides accuracy, the greatest utility of this analytical tool is its quickness and readiness for routine engineering analyses.

In 2021, Yang et al. [19] introduce a novel stepped shaft PDS. The new design features a conventional four-blade PDS assembly with a shaft containing two unique "steps" aligned with the first and third blades of the PDS. The steps create a reduced clearance at these locations, thus ensuring a leakage reduction. The authors present experimentally derived and CFD predicted leakage and force coefficients for the novel design and an identical smooth journal PDS. The results indicate the direct dynamic stiffness turns negative when switching from a smooth to stepped journal. More importantly, the authors illustrate the superior damping performance of the

stepped shaft PDS, whose effective damping is nearly 1.5 times larger than that of a uniform clearance PDS at an excitation frequency of 20 Hz.

Operating under a wet gas condition, the present research utilizes the same stepped rotor in Yang et al. [19] to further quantify the performance of a PDS with comparison to a similarly dimensioned LS.

Description of Test Rig and Test Seals

Test Rig Description

The two-phase flow (wet gas) test rig has a long history of providing experimentally derived seal dynamic force coefficients at Texas A&M University. San Andrés et al. [20,21,22] provide an in-depth description of the design of the wet gas test rig. Figure 2 illustrates the wet gas test rig under its current configuration. At the center of the test rig is a seal cartridge that contains the seal being tested, either a PDS or a LS. At the top of the seal cartridge lies a quick-disconnect adapter that attaches to a hose which supplies the test seal with a mixture of pressurized oil and air. Four equally spaced cylindrical rods support the seal cartridge. The structural properties (stiffness, damping, and mass) of the seal cartridge and support rods are known, allowing for the identification of the dynamic response of the test seal to external force excitations. Two orthogonally positioned electromagnetic shakers induce frequency dependent excitation forces onto the seal cartridge, thus exciting the oil and air mixture flow within the test seal.
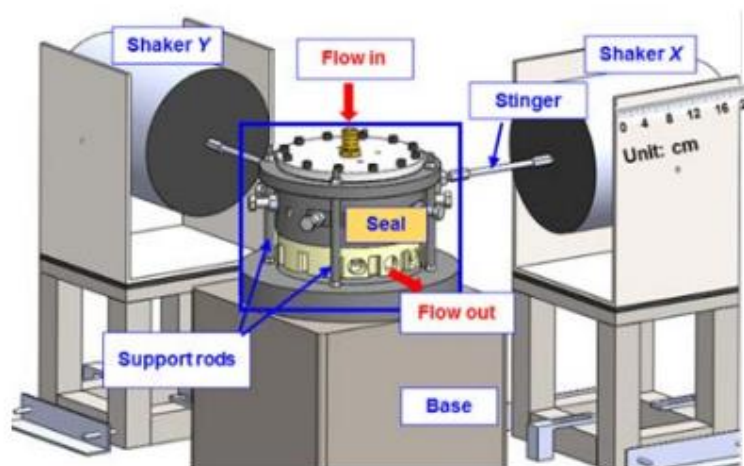
Fig. 2: Schematic of Wet Gas Seal Test Rig [22].

Figure 3 presents a cross-sectional view of the test seal cartridge. Both the stepped PDS and the stepped LS have a total length $L = 0.048$ m while the rotor diameter is $D = 2R = 0.127$ m. The PDS and LS differ slightly in radial clearance due to a manufacturing error. The PDS has a radial clearance $C_{r,PDS} = 0.196$ mm while the LS has a radial clearance $C_{r,LS} = 0.23$ mm, i.e. 17% larger.

Four centering bolts located along the outside of the seal cartridge move and position the test seal concentric with the center of a journal. In Fig. 3, the flow of wet gas is depicted with arrows, beginning at the quick-disconnect adapter and ending at the discharge chamber. A porous metal mixing sparger with pore size of 2 μm directly upstream of the quick-disconnect adaptor mixes dry air and ISO-VG10 oil to create a liquid in gas mixture. A 0-6.9 bar(g) pressure transducer threaded into the top lid (not depicted in Fig. 3) measures the supply pressure of the wet gas prior to entering the plenum upstream of the test seal.
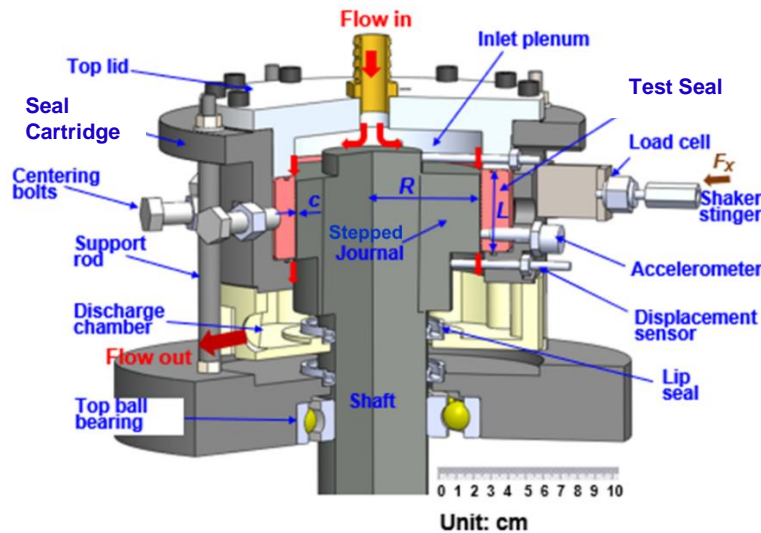
Fig. 3: Cross-Sectional View of Seal Cartridge Showing the Mixture Flow Path [22].

Upstream of the sparger element are two separate supply lines, one for the oil and one for dry air, as depicted in Fig. 4. A supply pump draws from the oil reservoir and moves oil through the supply line. Downstream of the pump lies a flow control valve and a flow meter with a range of 0.1 to 10 gallons per minute. The control valve allows for adjustment of oil flow to achieve the desired mixture composition. Regular shop air supplies an upstream pressure of 8.3 bar(g) into the dry air supply line. The air filter/dryer system removes any contamination or moisture from the shop air. The turbine flow meter requires a pressure of 6.9 bar(g) for accurate measurement of air volumetric flow rate. Therefore, a pressure regulator is positioned directly upstream of the turbine flow meter to reduce the air pressure from 8.3 to 6.9 (bar)g. Lastly, the air flow control valve

directly downstream of the turbine flow meter modulates the flow of air. When used in conjunction with the oil flow control valve, the air flow control valve allows for the adjustment of wet gas composition and supply pressure.
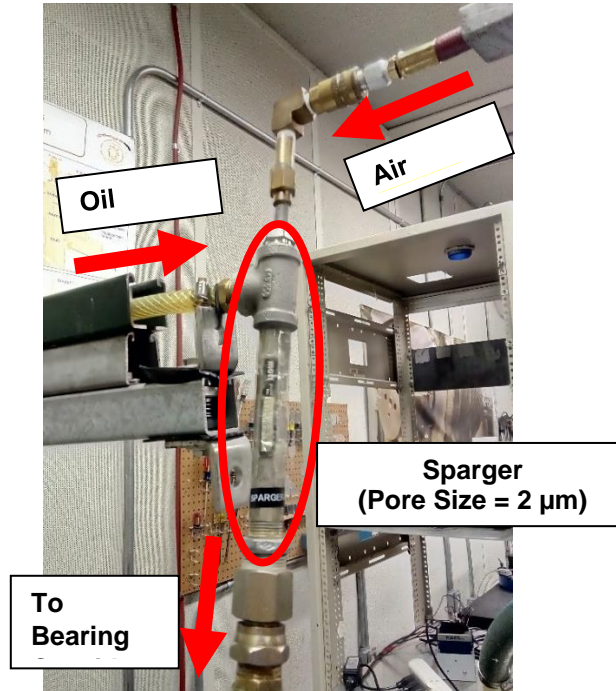
Fig. 4: Sparger Element Mixing Two Separate Supply Lines for Oil and Air.

The test seal cartridge hosts pairs of orthogonally placed piezoelectric accelerometers, eddy current displacement probes, and load cells. Figure 3 depicts the installation locations of the aforementioned sensors that measure the acceleration of the test seal, the displacement of the test seal with respect to the concentric journal, and the load applied to the test seal by the electromagnetic shakers, in two orthogonal directions, respectively. The manner in which the electromagnetic shakers connect to the load cells using stingers is shown in in Fig. 3. Figure 2 also show the stingers connecting to the aforementioned electromagnetic shakers. The oil in air mixture flowing between the journal and test seal as well as the support structure produce reactions to the applied dynamic loads.

Figure 5 depicts a cross-sectional view of the stepped journal, illustrating the nominal diameter and the diameter at the step locations. Note the slightly larger diameter at the step locations, and that produce a local reduced clearance when the seal is installed. The stepped journal is connected to a spinning shaft supported by two ball bearings with a top speed of 5,250 rpm that simulates actual operating conditions of a wet gas compressor system. A second oil pump draws oil from the

oil reservoir to lubricate and cool the two ball bearings during the experimentation. The shaft is driven by a pulley and belt located underneath the base that connects to an electric motor. The gear ratio between the electric motor and the shaft is 1.8. The electric motor is a refurbished jet engine starter with a rated top speed of 8,000 rpm. Flexible tubing connected to local shop air circulates pressurized air from underneath the electric motor in order to cool the motor during operation. A key phasor along with a piece of reflective tape positioned on the electric motor drive wheel provide accurate readings of the motor rotational speed.
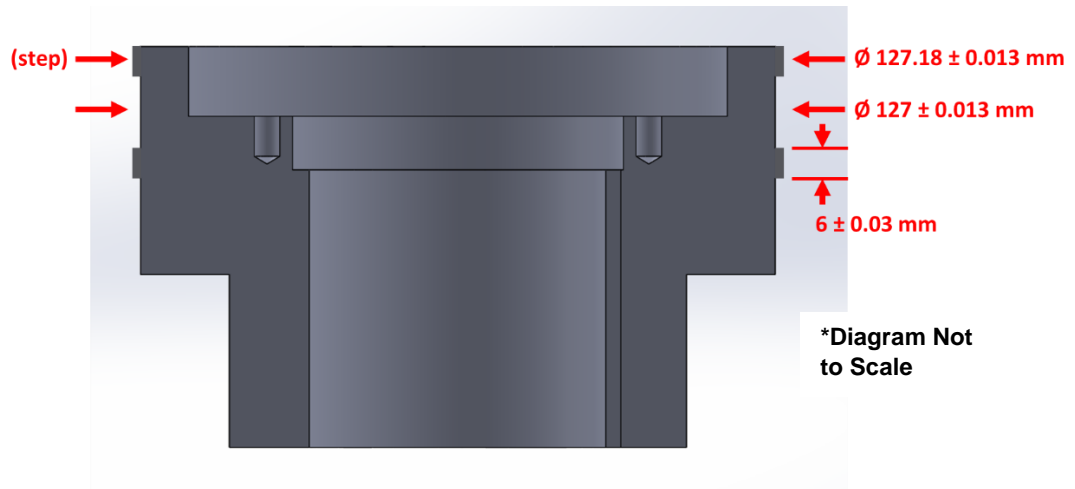
Fig. 5: Cross-sectional View of Stepped Journal (Not to Scale).

Description of Test Seals

The stepped PDS and stepped LS have similar dimensions to provide a vis-à-vis comparison of their performance. Table 1 presents the dimensions of both seals. Both seals have the same length L, journal diameter D, and cavity depth d, although featuring slightly different radial clearances C_r. The primary differences between the two seals lie in the thickness of the blades (ribs) and the width of the cavities/pockets.

Table 1: Geometry of Stepped Seals

Stepped Pocket Damper Seal		Stepped Labyrinth Seal	
Seal Length, L	48 ±0.03 mm	Seal Length, L	48 ±0.03 mm
Journal Diameter, D	127 ±0.013 mm	Journal Diameter, D	127 ±0.013 mm
*Seal Clearance, $C_{r,PDS}$	0.196 ±0.007 mm	*Seal Clearance, $C_{r,LS}$	0.230 ±0.007 mm
*Seal Clearance (step), $C_{r,step,PDS}$	0.106 ±0.007 mm	*Seal Clearance (step), $C_{r,step,LS}$	0.140 ±0.007 mm
Pocket/Cavity Depth, d	4.8 ±0.03 mm	Cavity Depth, d	4.8 ±0.03 mm
Pocket/Cavity Width	10.5/4.8 ±0.03 mm	Cavity Width	11.6 ±0.03 mm
Rib Width	2.5 ±0.03 mm	Tip Thickness	0.2 ±0.03 mm

*Measured at 21°C

Figures 6 (a) and (b) present 3D models and cross-sectional diagrams illustrating the direction of flow and dimensions of the various features in the stepped PDS and stepped LS respectively. The PDS, made of 6061-T6 aluminum alloy, features four blades, sectioning off the seal into three rows of cavities. The center cavity has a width of 4.8 mm, whereas the other cavities are 10.5 mm wide. All PDS pockets and cavities have a depth of 4.8 mm. All blades and partition walls for the PDS are 2.5 mm in thickness. A total of eight partition walls are positioned between two adjacent blades, dividing each cavity into eight equally spaced pockets. Note that Fig. 6 depicts the two "steps" machined into the journal, as in the design introduced by Yang et al. [19] in 2020. Prior testing reveals a decrease in seal leakage and a significant increase in direct damping when compared to a uniform clearance PDS [19].

Figure 6 (b) presents a 3D model and cross-sectional diagram of the similarly dimensioned stepped LS. The LS, made of 6061-T6 aluminum alloy, consists of three equally spaced cavities with a width of 11.6 mm and a depth of 4.8 mm. Each blade of the LS is angled at 5 degrees and has a tip width of 2.5 mm. Note the stepped shaft is also used with the LS.
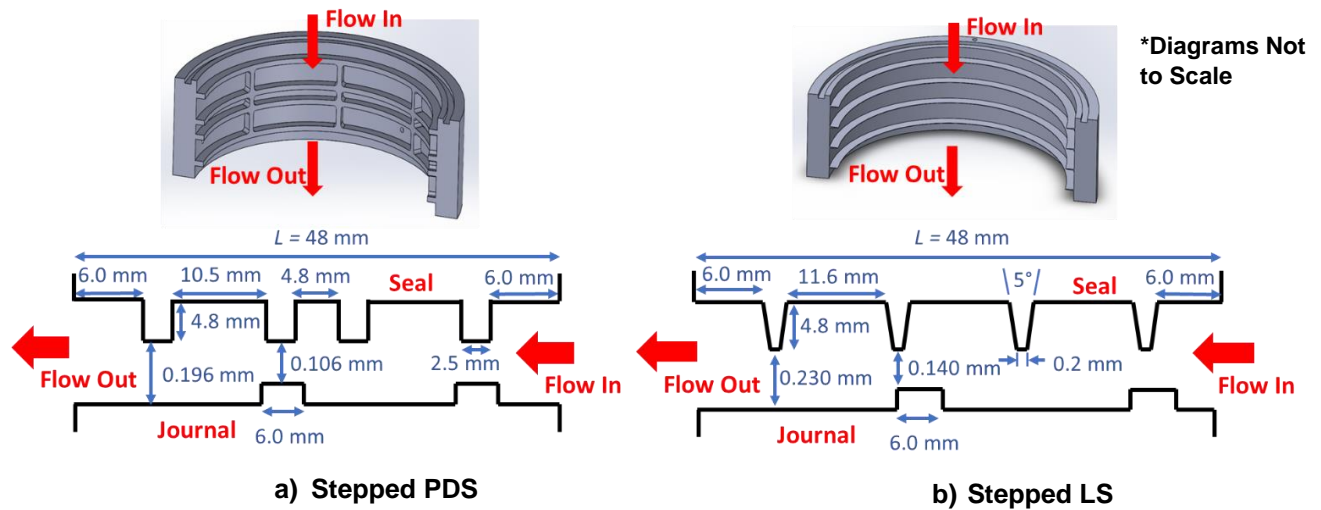
Fig. 6: Cross-Sectional Diagrams Illustrating Dimensions of (a) Stepped PDS and (b) Stepped LS (Not to Scale).

Experimental Procedure

Measurements of Seal Leakage

Seal leakage measurements took place for a variety of operating conditions. Prior to measuring leakage, a test seal is installed and centered within its cartridge. Using feeler gauges to determine the clearance, the centering bolts position the seal to achieve a uniform clearance between the journal and seal.

For each experiment, the target supply pressure (P_s), liquid volume fractions (LVF), and journal speed at which the leakage is to be measured are clearly stated. Table 2 provides a summary of the lubricant properties and operating conditions controlled during these experiments.

Table 2: Lubricant Properties, and Operating Conditions

Oil Type:	ISO-VG10
Density, ρ_{oil}	861 kg/m^3
Viscosity, μ_{oil}	15.6 cP (at 294 K)
Density, ρ_{air}	1.185 kg/m^3 (at 1 bar(a), 294 K)
Viscosity, μ_{air}	0.018 cP (at 294 K)
Mixture Supply Temp, T_s.	294 K
Liquid Volume Fraction, LVF	0.0-0.10
Supply Pressure, P_s	2.5, 3.3, 4.2 bar(a)
Exit Pressure, P_e	1 bar(a)
Journal Speed, Ω	0, 3000, 5250 rpm
Surface Speed, $u = \frac{1}{2} D \Omega$	0, 19.9, 34.9 m/s

During an experiment, the motor and pulley system bring the journal to a target speed. Figure 7 outlines the procedure to measure seal leakage for a given P_s, LVF range, and journal speed. Note that this procedure initially calls for fully opening the air flow control valve, thus allowing for just air to flow through the test seal. Afterwards, oil is slowly added into the mixture until reaching the target supply pressure. Calculation of the seal leakage and mixture LVF follow once the target P_s is achieved.

Fig. 7. Experimental Procedure for Measurement of Seal Leakage at a Target Supply Pressure, LVF Range, and Rotor Speed.

Seal leakage ($\dot{m}$) equals the sum of the measured air mass flow rate ($\dot{m}_{air}$) and oil mass flow rate ($\dot{m}_{oil}$):

$$\dot{m} = \dot{m}_{air} + \dot{m}_{oil} \tag{1}$$

The air flow meter delivers the volumetric flow rate of air (Q_{air}), hence:

$$\dot{m}_{air} = Q_{air}\, \rho_{air} \tag{2}$$

where ρ_{air} is the air density at the given supply pressure P_s and temperature T_s. The air flow meter displays readings in standard conditions and is converted to volumetric flow rate at the supply conditions by:

$$Q_{air} = Q_{air,\,standard} \left(\frac{14.7\ \text{psia}}{P_s} \right) \left(\frac{T_s}{520°\text{R}} \right) \tag{3}$$

19

Similar to the air mass flow rate, the oil mass flow rate equals:

$$\dot{m}_{oil} = Q_{oil}\,\rho_{oil} \tag{4}$$

The LVF of a gas and liquid mixture equals the ratio of the volume of the liquid to the total volume of the mixture.

$$LVF = \frac{Q_{oil}}{Q_{air} + Q_{oil}} = (1 - GVF) \tag{5}$$

where GVF denotes the mixture gas volume fraction, the ratio of gas volumetric flow rate to total mixture volumetric flow rate. Next, following the procedure outlined in Fig. 7, the operator reduces the flow of air by closing the air flow control valve. After, the oil flow increases until the target supply pressure is once again achieved. These two steps serve to increase the LVF while maintaining the target supply pressure. The procedure of decreasing air and increasing oil is repeated until measurements have taken place throughout the entire range of LVF at the specified supply pressure and journal speed.

Identification of Force Coefficients

San Andrés [23] details the procedure for identifying the dynamic force coefficients of mechanical systems. The test seal and its stator are represented as a lumped mass (M_{sc}), displacing along two degrees of freedom (x, y). Figure 8 provides a representation of the test seal with springs and dashpots denoting the stiffness (K) and damping (C) coefficients of the test seal. K_h and C_h represent the stiffness and damping of the support structure respectively.

The elastic support structure and test seal react to dynamic forces applied to the seal stator, while the spinning journal is assumed to be rigid. The response of the test seal to a dynamic load is a function of the properties of the oil and air mixture flowing between the seal and the journal and the excitation frequency. Note that K_{ij} and C_{ij} in Fig. 8 represent stiffness and damping coefficients produced by a change in force along the "i" direction due to a motion in the "j" direction.

20
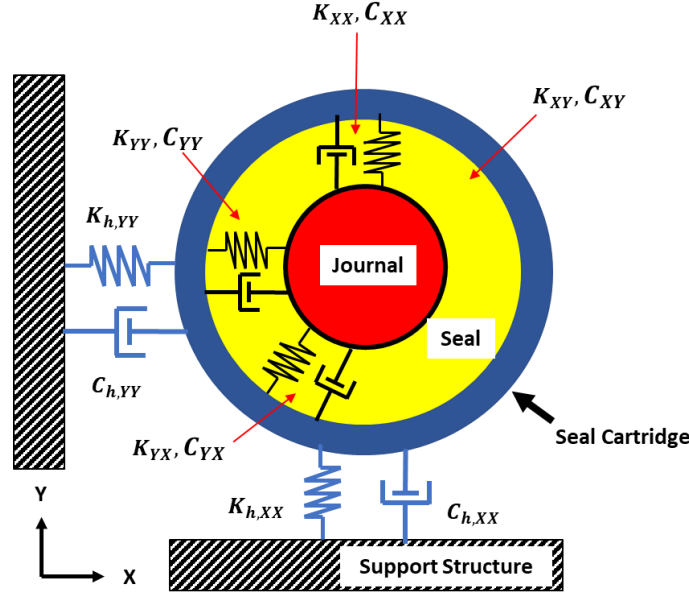
Fig. 8. Representation of Lumped Mass with Two Degrees of Freedom Assumption Used in Identification of Force Coefficients [23].

The equations of motion for the mechanical system described in Fig. 8 [23] are:

$$M_{sc}\,\ddot{x}+\left(C_{xx}+C_{h,xx}\right)\dot{x}+C_{xy}\,\dot{y}+\left(K_{xx}+K_{h,xx}\right)x+K_{xy}\,y=f_{x}$$

$$M_{sc}\,\ddot{y}+\left(C_{yy}+C_{h,yy}\right)\dot{y}+C_{yx}\,\dot{x}+\left(K_{yy}+K_{h,yy}\right)y+K_{yx}\,x=f_{y} \qquad (6)$$

where $M_{sc}=14$ kg represents the equivalent mass of the seal stator, and f_x and f_y represent dynamic force excitations applied to the stator by the electromagnetic shakers.

San Andrés [23] provides a step-by-step procedure to identify the dynamic force coefficients of the system. The first step consists of applying two separate and independent force excitations to the seal stator. These excitations are known dynamic loads exerted at a single frequency. The first excitation consists of a force entirely in the *x*-direction while the second excitation consists of a force entirely in the *y*-direction:

$$\mathbf{F_1}=\begin{bmatrix} f_{x1} \\ 0 \end{bmatrix},\ \mathbf{F_2}=\begin{bmatrix} 0 \\ f_{y2} \end{bmatrix} \qquad (7)$$

Sensors record the displacement and acceleration of the seal cartridge with respect to the fixed journal and the dynamic load applied by the electromagnetic shakers.

Let $\mathbf{D_1}$, $\mathbf{D_2}$, $\mathbf{A_1}$, and $\mathbf{A_2}$, denote the measured displacement and acceleration in two orthogonal directions of the seal stator over a set period of time:

$$\mathbf{D_1} = \begin{bmatrix} x_1 \\ y_1 \end{bmatrix}, \mathbf{D_2} = \begin{bmatrix} x_2 \\ y_2 \end{bmatrix}$$

$$\mathbf{A_1} = \begin{bmatrix} \ddot{x}_1 \\ \ddot{y}_1 \end{bmatrix}, \mathbf{A_2} = \begin{bmatrix} \ddot{x}_2 \\ \ddot{y}_2 \end{bmatrix} \tag{8}$$

$\overline{\mathbf{F}}$, $\overline{\mathbf{D}}$, and $\overline{\mathbf{A}}$ denote the amplitudes of the discrete Fourier transform (DFT) of the measured dynamic loads, displacements, and accelerations:

$$\overline{\mathbf{F}}_1 e^{i\omega t} = \text{DFT}(\mathbf{F_1}) = \begin{bmatrix} \overline{F}_{x1} \\ 0 \end{bmatrix}, \overline{\mathbf{F}}_2 e^{i\omega t} = \text{DFT}(\mathbf{F_2}) = \begin{bmatrix} 0 \\ \overline{F}_{y2} \end{bmatrix}$$

$$\overline{\mathbf{D}}_1 e^{i\omega t} = \text{DFT}(\mathbf{D_1}) = \begin{bmatrix} \overline{x}_1 \\ \overline{y}_1 \end{bmatrix}, \overline{\mathbf{D}}_2 e^{i\omega t} = \text{DFT}(\mathbf{D_2}) = \begin{bmatrix} \overline{x}_2 \\ \overline{y}_2 \end{bmatrix} \tag{9}$$

$$\overline{\mathbf{A}}_1 e^{i\omega t} = \text{DFT}(\mathbf{A_1}) = \begin{bmatrix} \overline{a}_{x1} \\ \overline{a}_{y1} \end{bmatrix}, \overline{\mathbf{A}}_2 e^{i\omega t} = \text{DFT}(\mathbf{A_2}) = \begin{bmatrix} \overline{a}_{x2} \\ \overline{a}_{y2} \end{bmatrix}$$

Substituting Eq. (9) into Eq. (6) provides the equations of motion related to the two independent force excitations rewritten in the frequency domain:

$$\begin{bmatrix} \left[(K_{xx}+K_{h,xx})+(C_{xx}+C_{h,xx})i\omega\right] & \left[K_{xy}+C_{xy}i\omega\right] \\ \left[K_{yx}+C_{yx}i\omega\right] & \left[(K_{yy}+K_{h,yy})+(C_{yy}+C_{h,yy})i\omega\right] \end{bmatrix} \begin{bmatrix} \overline{x}_1 \\ \overline{y}_1 \end{bmatrix} = \begin{bmatrix} \overline{F}_{x1} \\ 0 \end{bmatrix} -M_{sc}\begin{bmatrix} \overline{a}_{x1} \\ \overline{a}_{y1} \end{bmatrix}$$

$$\begin{bmatrix} \left[(K_{xx}+K_{h,xx})+(C_{xx}+C_{h,xx})i\omega\right] & \left[K_{xy}+C_{xy}i\omega\right] \\ \left[K_{yx}+C_{yx}i\omega\right] & \left[(K_{yy}+K_{h,yy})+(C_{yy}+C_{h,yy})i\omega\right] \end{bmatrix} \begin{bmatrix} \overline{x}_2 \\ \overline{y}_2 \end{bmatrix} = \begin{bmatrix} 0 \\ \overline{F}_{y2} \end{bmatrix} -M_{sc}\begin{bmatrix} \overline{a}_{x2} \\ \overline{a}_{y2} \end{bmatrix}$$

$$\tag{10}$$

Expressing Eq. (10) in matrix forms allows for the introduction of the complex dynamic stiffness matrix $\mathbf{H}$:

$$\mathbf{H}\begin{bmatrix} \overline{x}_1 & \overline{x}_2 \\ \overline{y}_1 & \overline{y}_2 \end{bmatrix} = \begin{bmatrix} \overline{F}_{x1} & 0 \\ 0 & \overline{F}_{y2} \end{bmatrix} - M_{sc}\begin{bmatrix} \overline{a}_{x1} & \overline{a}_{x2} \\ \overline{a}_{y1} & \overline{a}_{y2} \end{bmatrix} \tag{11}$$

$\mathbf{H}$ is a 4x4 matrix containing the stiffness $(K_{ij})_{i,j=x,y}$ and damping $(C_{ij})_{i,j=x,y}$ coefficients,

$$\mathbf{H} = \mathbf{K}_{(\omega)} + i\omega\mathbf{C}_{(\omega)} \qquad (12)$$

Eq. (11) is four equations and four unknowns and can readily be solved with simple matrix algebra. The solution renders the matrix of dynamic stiffnesses $\mathbf{H}_k$ at each frequency ω_k. Note that the dynamic stiffness is a complex number. The real portion of $\mathbf{H}$ represents the dynamic stiffness of the system due to both the structure and the test seal. Similarly, the imaginary portion of $\mathbf{H}$ represents the damping of the system due to both the structure and the test seal. It can be seen from Eq. (10) that extracting the test seal force coefficients requires that the stiffness and damping coefficients of the structure be known. Appendix A provides a description of the technique used in identifying the structure force coefficients.

Experimental Results

This section presents the experimental results for the leakage and rotordynamic force coefficients of the stepped PDS and the stepped LS supplied with a wet gas. The figures below depict direct comparisons of the leakage for both seals supplied with an oil in air mixture. An orifice-like loss coefficient (C_d) quantifies the effectiveness of both seals to restrict leakage. Next, the real and imaginary parts of the direct complex dynamic stiffness coefficients (H), the real part of the cross-coupled complex dynamic stiffness coefficients (h), and an effective damping coefficient (C_{eff}) shown against the excitation frequency (ω) provide a comparison of the rotordynamic performance.

Leakage

Let $\dot{m}$ represent the total mass flow rate through the test seal, either the stepped PDS or stepped LS, and C_e represent an effective radial clearance of an equivalent single-restriction seal. Derived from Bernoulli's equation, the mass flow rate through the equivalent seal is [24]:

$$\dot{m} = \bar{\rho}\, A\, v = (\pi\, D\, C_e)\sqrt{2\,\bar{\rho}\,(P_s - P_e)} \qquad (13)$$

where v denotes the fluid velocity and $A = (\pi\, D\, C_e)$ denotes the flow cross-sectional area. For pure gas flow, the density ($\bar{\rho}$) is a function of the arithmetic average of the seal inlet and exit pressures,

$$\bar{\rho} = \frac{P_s + P_e}{2\, R_g\, T} \qquad (14)$$

where R_g represents the specific gas constant of air and T is the flow temperature. The seal effective clearance (C_e) is equivalent to the physical seal clearance (C_r) multiplied by an orifice-like loss coefficient (C_d):

$$C_e = (C_d\,C_r) \tag{15}$$

Substituting Eq. (15) into Eq. (13) provides the recorded mass flow rate ($\dot{m}$) as a function of the seal loss coefficient (C_d):

$$\dot{m} = C_d\,(\pi\,D\,C_r)\sqrt{2\,\bar{\rho}\,(P_s\text{-}P_e)} = C_d\,\dot{m}_{ideal} \tag{16}$$

Thus, C_d relates the actual measured mass flow rate ($\dot{m}$) to the flow rate ($\dot{m}_{ideal}$) of an idealized single-restriction seal with radial clearance C_r supplied with an ideal fluid with no viscosity. C_d quantifies the effectiveness of a seal to reduce leakage; a lower C_d denotes a more effective seal.

San Andrés et al. [24] also use a modified flow factor $\bar{\emptyset}$ to characterize the leakage of a seal related to its inlet pressure (P_s), exit pressure (P_e), temperature (T), and seal geometry:

$$\bar{\emptyset} = \frac{\dot{m}\sqrt{T}}{D\,P_s\sqrt{1-\left(\frac{P_s}{P_e}\right)^2}} = \pi\,C_d\,C_r\,\frac{1}{\sqrt{R_g}} \tag{17}$$

Figure 9 presents the leakage ($\dot{m}$), modified flow factor ($\bar{\emptyset}$) and loss coefficient (C_d) for the stepped PDS and stepped LS operating with just air (LVF = 0%). The ratio of supply pressure to exit pressure (P_s/P_e) ranges from 1.2 to 2.7. Figure 9 shows the stepped PDS has a lower $\dot{m}$ and a lower $\bar{\emptyset}$, as the radial clearance of the stepped LS ($C_{r,LS}$ = 0.230 mm) is larger than that of the stepped PDS ($C_{r,PDS}$ = 0.196 mm). The results show $\dot{m}$ is insensitive to journal speed, indicating the axial flow velocity is much greater than the circumferential flow velocity. The average cross-film circumferential flow velocity $V_c = \frac{U}{2} = 17.5$ m/s for a journal speed of 5250 rpm, whereas the exit axial flow velocity $V_e = \frac{\dot{m}}{\rho_e\,A} = 74$ m/s for the lowest recorded $\dot{m}$ of the stepped PDS.

Recall that C_d is an indicator of the seal effectiveness to reduce leakage; a lower C_d representing a more effective seal. Interestingly, the stepped PDS produces a lower C_d. The $C_{d,PDS}$ = 0.23 for the stepped PDS and is constant vs. (P_s/P_e), whereas $C_{d,LS}$ = 0.33.

(a) $\dot{m}$ vs. P_s/P_e

(b) $\bar{\phi}$ vs. P_s/P_e

(c) C_D vs. P_s/P_e
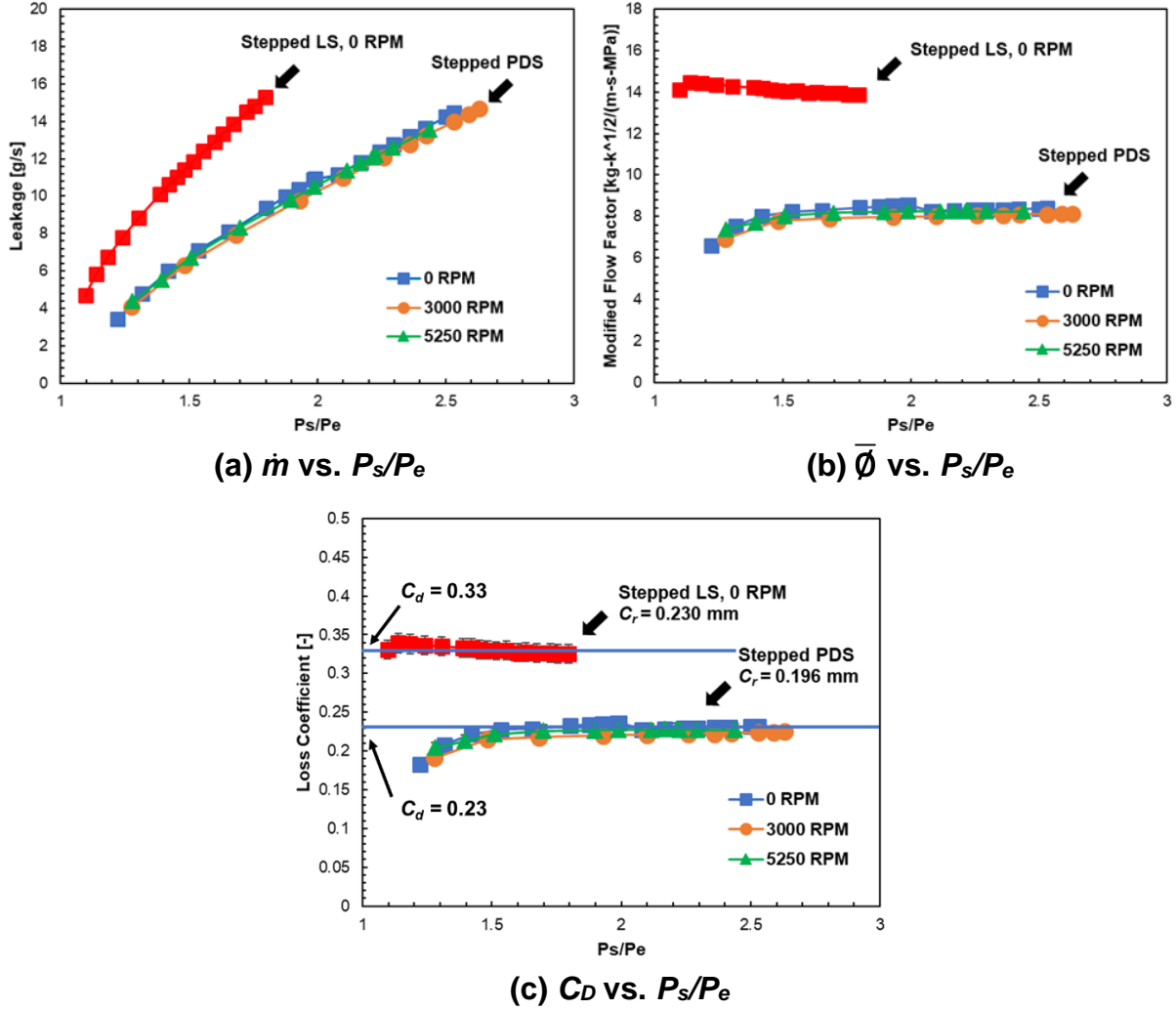
Fig. 9. Leakage ($\dot{m}$), Modified Flow Factor ($\bar{\phi}$), and Loss Coefficient (C_D) vs Pressure Ratio (P_s/P_e) for a Stepped PDS and a Stepped LS Operating with Air. Journal Speed = 0, 3000, and 5250 rpm.

For a mixture of oil and air, the average mixture density ($\bar{\rho}_m$) is a function of the LVF:

$$\bar{\rho}_m = (1 - \text{LVF})\, \bar{\rho}_{air} + \text{LVF}\, \rho_{oil} \tag{18}$$

where $\bar{\rho}_{air} = \dfrac{P_s + P_e}{2\,R_g\,T}$ represents the average air density. Substituting Eq. (18) into Eq. (16) produces a loss coefficient (C_d) for the two-phase flow condition.

Figure 10 presents the leakage ($\dot{m}$), modified flow factor ($\bar{\phi}$) and loss coefficient (C_d) for both the stepped PDS and stepped LS operating with $P_s/P_e = 2.5$ and a LVF ranging from 0% to 6%. Notice the C_d of the stepped LS supplied with a two-phase flow is greater than that of the

25

stepped LS supplied with air alone. Conversely, the C_d for the stepped PDS supplied with a two-phase flow is smaller than that of the stepped PDS supplied with just air (LVF = 0%).

$P_s/P_e = 2.5$

(a) $\dot{m}$ vs. LVF
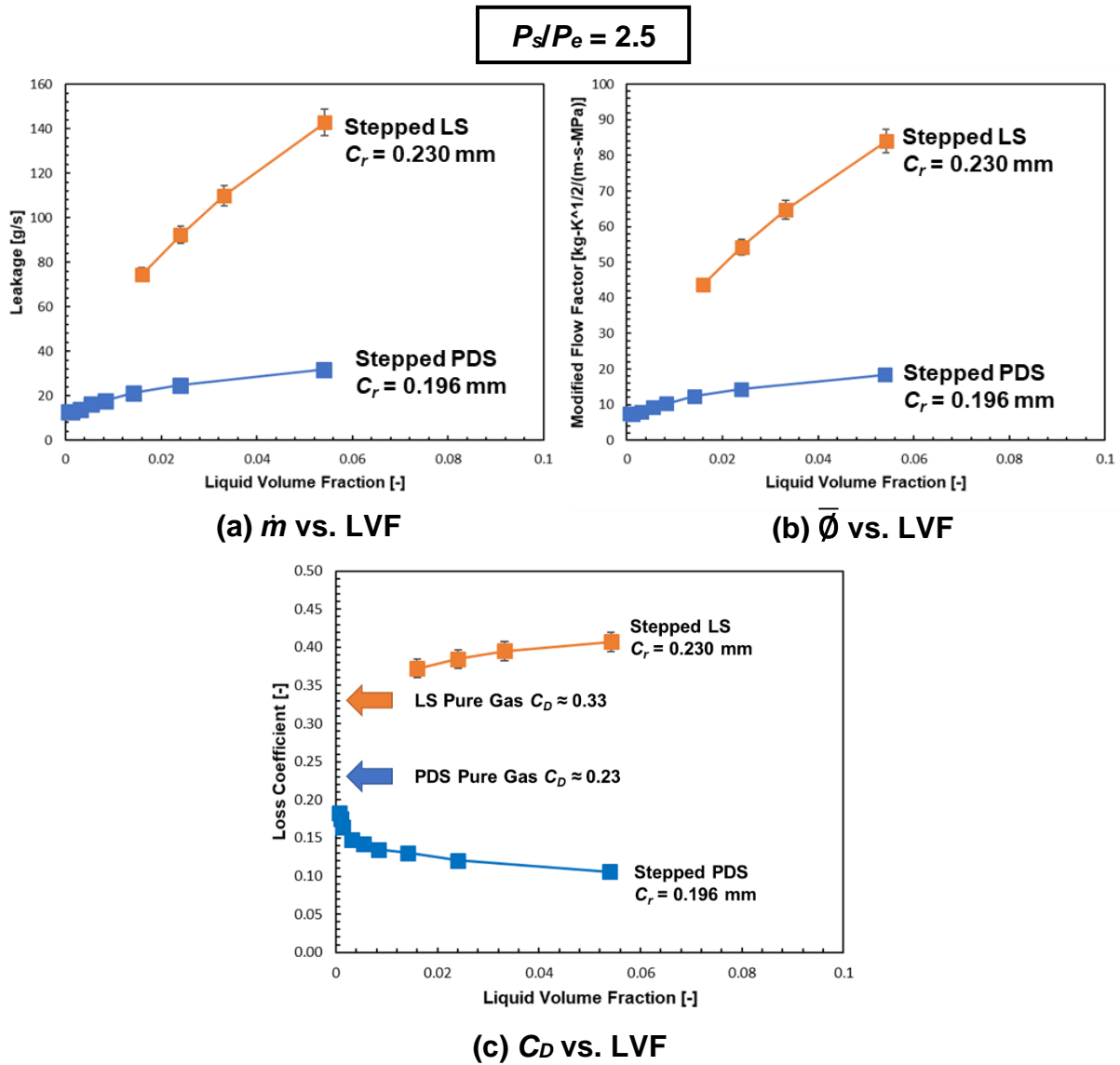
(b) $\bar{\bar{\varnothing}}$ vs. LVF

(c) C_D vs. LVF

Fig. 10. Leakage ($\dot{m}$), Modified Flow Factor ($\bar{\bar{\varnothing}}$), and Loss Coefficient (C_D) vs LVF of Stepped PDS and Stepped LS. Journal Speed = 0 rpm and $P_s/P_e = 2.5$.

Figures 11 and 12 present the leakage ($\dot{m}$) and loss coefficient (C_d) for the stepped PDS supplied with a two-phase flow, respectively. The LVF ranges from 0% to 10%, $P_s/P_e = 2.5$, 3.3, and 4.2 bar(a), and the journal speed = 0, 3000, and 5250 rpm. As more oil is added into the mixture (LVF increases), C_d tends to decrease in magnitude. This is attributed to the rapid increase in mixture density ($\bar{\rho}_m$). As more air is added to the flow mixture (LVF decreases), C_d increases towards the pure gas $C_d = 0.23$ depicted in Fig. 9 (c).

26
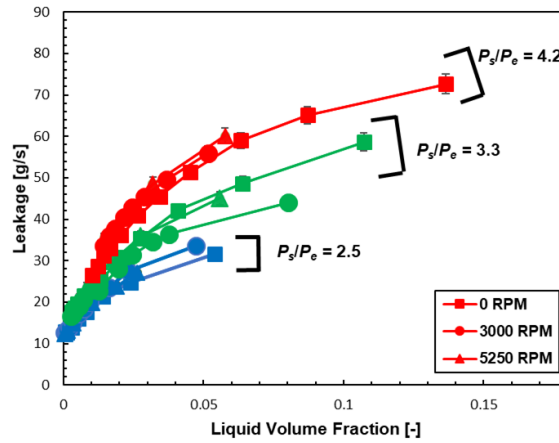
Fig. 11. Leakage ($\dot{m}$) vs. LVF for Stepped PDS Operating with Two-Phase Flow. Journal Speed = 0, 3000, and 5250 rpm, P_s/P_e = 2.5, 3.3, and 4.2.

(a) 0 RPM
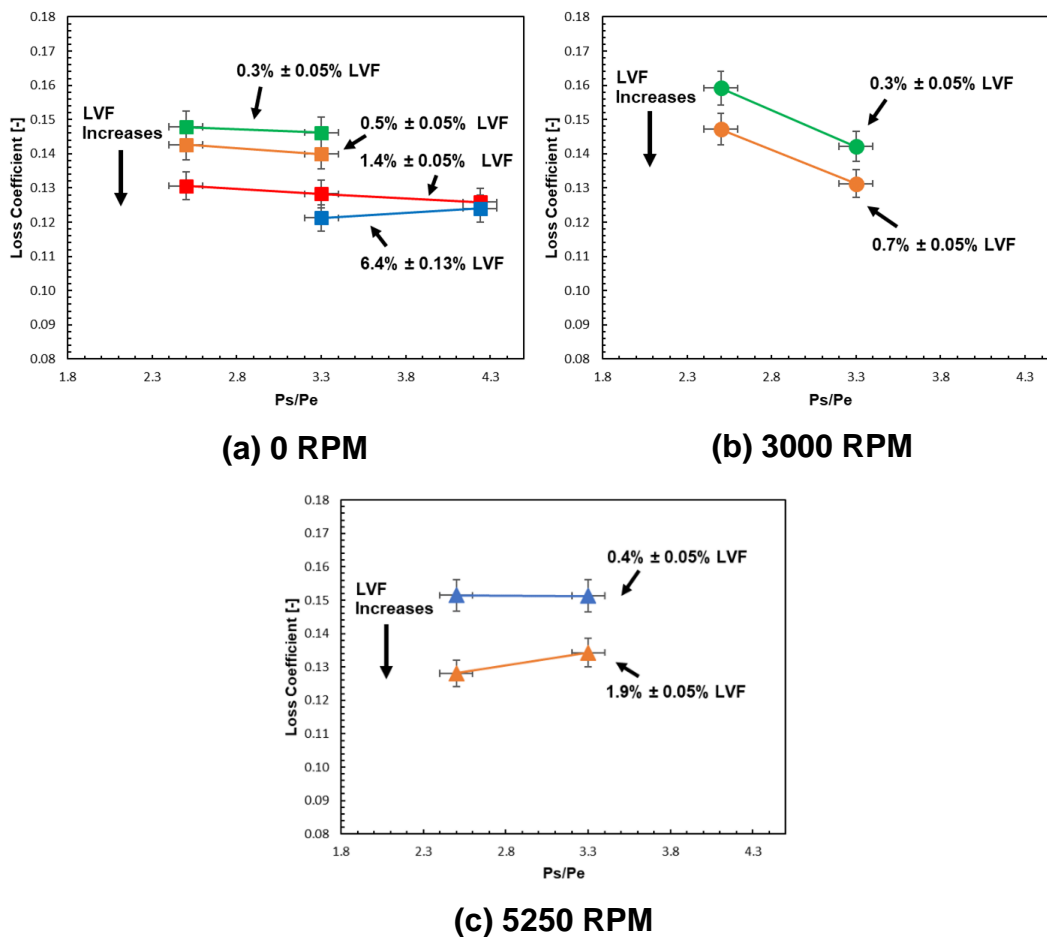
(b) 3000 RPM

(c) 5250 RPM

Fig. 12. Loss Coefficient (C_D) vs Pressure Ratio (P_s/P_e) for Stepped PDS Operating with Two-Phase Flow. Journal Speed = (a) 0, (b) 3000, and (c) 5250 rpm.

Table 3 provides the measured leakage and liquid mass fraction (LMF) of the stepped PDS and stepped LS operating with a LVF = 1.3%, P_s/P_e = 2.35, and journal speed = 0, 3000, and 5250 rpm. The stepped LS allows a substantially higher air and oil mixture flow rate compared to that

27

of the stepped PDS. Recall the stepped LS has a larger radial clearance and lower effectiveness (higher C_d). Notice that although the mass flow rate is much greater, the liquid mass fraction, defined as the ratio of liquid mass flow rate to the total mass flow rate, remains nearly the same across all tests. The total flow rate for the stepped LS is consistently more than thrice that of the stepped PDS.

Table 3: Measured Leakage for Air and Oil of a Stepped PDS and a Stepped LS. Operation with LVF = 1.3% ± 0.05%, P_s/P_e = 2.35.

	Journal Speed, Ω [rpm]	Total Flow Rate $\dot{m}$ [g/s]	Air Flow Rate, $\dot{m}_{air}$ [g/s]	Oil Flow Rate $\dot{m}_{oil}$ [g/s]	GVF [%]	LVF [%]	LMF [%]
PDS	0 RPM	20.14±0.31	3.84±0.01	16.30±0.3	98.7±0.05	1.3±0.05	80.9±0.4
	3000 RPM	19.05±0.31	3.84±0.01	15.21±0.3	98.7±0.05	1.3±0.05	79.8±0.4
	5250 RPM	19.62±0.31	3.87±0.01	15.75±0.3	98.7±0.05	1.3±0.05	80.3±0.4
LS	0 RPM	67.57±1.14	13.25±0.04	54.32±1.1	98.7±0.05	1.3±0.05	80.4±0.4
	3000 RPM	64.13±1.14	13.07±0.04	51.06±1.1	98.8±0.05	1.2±0.05	79.6±0.4
	5250 RPM	66.53±1.14	13.30±0.04	53.23±1.1	98.7±0.05	1.3±0.05	80.0±0.4

Dynamic Force Coefficients

The experimental results indicate that the measured direct dynamic complex stiffnesses H_{xx} and H_{yy} are similar in magnitude, whereas the cross-coupled dynamic complex stiffnesses H_{xy} and H_{yx} are of similar magnitude and opposite sign; i.e. $H_{xx} \approx H_{yy}$ and $H_{xy} \approx - H_{yx}$. Thus, the following figures show the direct dynamic stiffness (H), the cross-coupled dynamic stiffness (h), and the effective damping coefficient (C_{eff}) as:

$$H = \frac{(H_{xx} + H_{yy})}{2} \; , \; h = \frac{(H_{xy} - H_{yx})}{2} \; , \; C_{eff} = \frac{(\mathrm{Ima}(H) - \mathrm{Re}(h))}{\omega} \tag{19}$$

Figure 13 presents the real and imaginary parts of H for both seals supplied with a two-phase flow vs. frequency. The LVF = 98.7% ± 0.05%, P_s/P_e = 2.35, and the journal speed = 0, 3000, and 5250 rpm (surface speed = 0, 20, 35 m/s). In the graphs, a vertical dashed lines denotes the synchronous frequency. Figure 13 reveals the stepped PDS consistently provides a greater amount of direct damping (corresponding to Ima(H)) when compared to the stepped LS. The stepped LS produces a negative Ima(H) at all excitation frequencies with few exceptions (low excitation frequencies and operation without journal rotation). Conversely, the stepped PDS produces a positive Ima(H) for all excitation frequencies.

The stepped PDS produces a larger direct stiffness (corresponding to Re(H)) than the stepped LS at frequencies above 60 Hz, and a lower stiffness at frequencies below 60 Hz. The

three sets of results reveal that Re(H) tends to decrease (slightly) as the journal speed increases from 0 rpm to 3000 and 5250 rpm, while Ima(H) shows an insensitivity to journal speed. One notable anomaly in the experimental results arises in the damping of the stepped PDS with the journal speed set to 3000 rpm, in which low frequency excitations resulted in unusually high Ima(H).
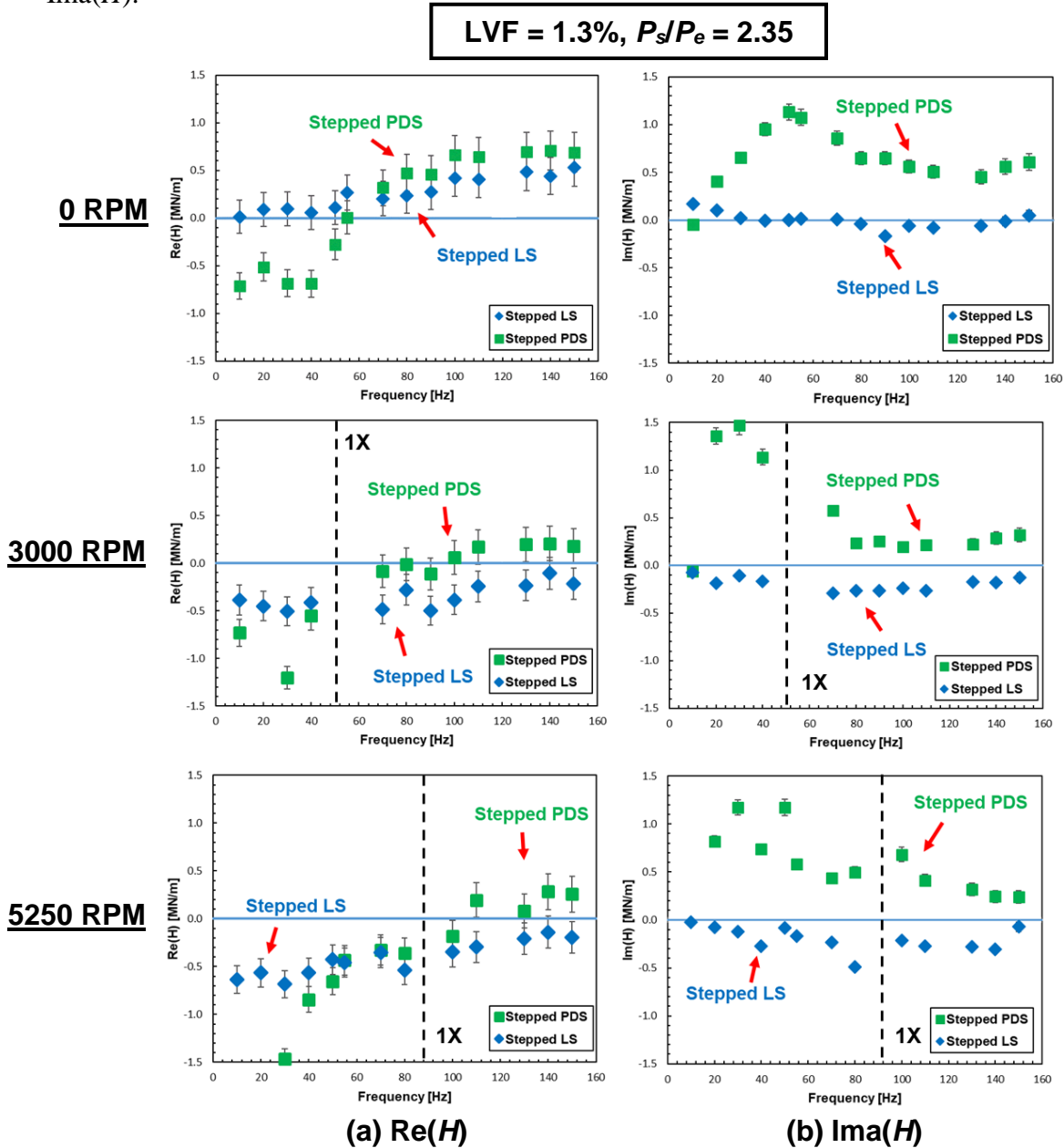
Fig. 13. Real and Imaginary Parts of Complex Direct Dynamic Stiffness (H) for a Stepped LS and a Stepped PDS. Operation with P_s/P_e = 2.35, LVF = 1.3% ± 0.05%, and Three Journal Speeds (0, 3000, and 5250 rpm).

Figure 14 presents the real part of the cross-coupled dynamic stiffness (h) and the effective damping coefficient (C_{eff}) vs. excitation frequency for both the stepped PDS and stepped LS

supplied with a two-phase flow. The LVF = 98.7% ± 0.05%, P_s/P_e = 2.35, and the journal speed = 0, 3000, and 5250 rpm (0, 50, and 88 Hz). Cross-coupled force coefficients (h) are very small, typically smaller than the experimental uncertainty. Note that the C_{eff} comprises of contributions from the direct damping (C) and the cross-coupled stiffness (h). With very small cross-coupled effects, the dominant factor in C_{eff} is the direct damping of the system. The stepped PDS produces a greater C_{eff} than the stepped LS at all excitation frequencies and for the three journal speeds.

(a) Re(h) **(b) C_{eff}**
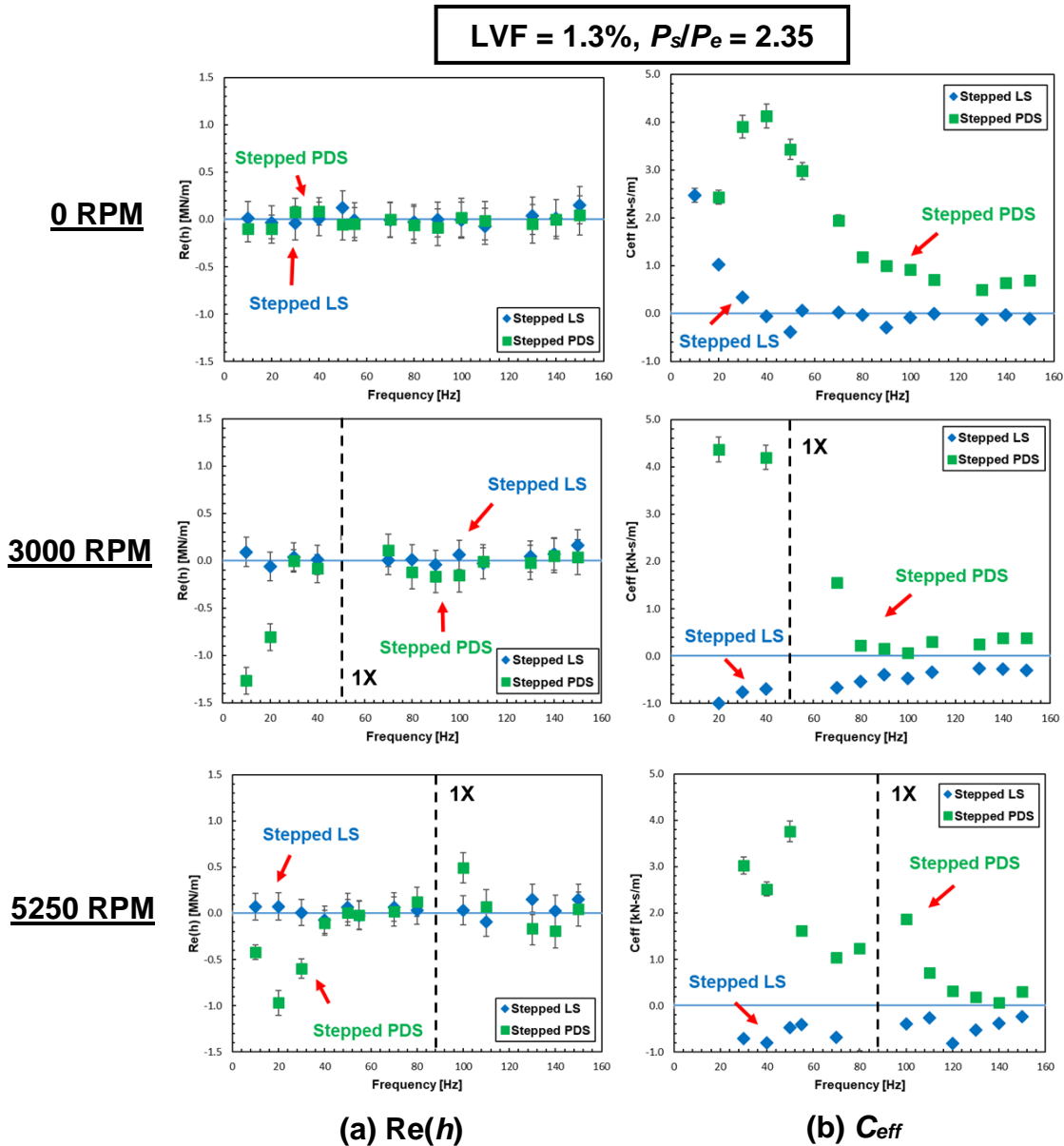
Fig. 14. Real Part of Cross-Coupled Complex Dynamic Stiffness (h) and Effective Damping Coefficient (C_{eff}) for a Stepped PDS and a Stepped LS. Operation with P_s/P_e = 2.35, LVF = 1.3% ± 0.05%, and Three Journal Speeds (0, 3000, and 5250 rpm).

Figure 15 presents the real and imaginary parts of the direct dynamic stiffness (H) for the stepped PDS operating with LVF = 0%, 0.4%, and 0.7%. The journal speed = 0, 3000, and 5250 rpm and P_s/P_e = 2.5. Regardless of the magnitude of journal speed, the results showcase that the effect of increasing the amount of liquid in the mixture on Re(H) depends on the excitation frequency. The results show that Re(H) tends to decrease at low frequencies (<80 Hz) as the LVF increases. Conversely, Re(H) tends to increase at high frequencies (>80 Hz) as the LVF increases. Increasing the LVF of the mixture tends to increase the Ima(H) for the stepped PDS at all excitation frequencies, likely due to the higher viscosity of the mixture.

The results presented in Fig. 15 for the stepped PDS operating with LVF = 0% and null journal speed indicate Re(H) > 0 for ω > 20 Hz. Previously, Yang et al. [19] present negative values for Re(H) for ω ranging from 20 to 120 Hz using a similarly dimensioned stepped PDS operating with LVF = 0% (gas only) and null journal speed. The magnitude of the results in Ref. [19] is very small, typically lesser than 0.1 MN/m.

Yang et al. [19] also present rotordynamic force coefficients of a similarly dimensioned uniform clearance PDS. The present results for the stepped PDS are similar to those for the uniform clearance PDS [19], indicating that Re(H) for journal speed = 0 rpm and LVF = 0% are small (<0.5 MN/m) and increase slightly as the excitation frequency (ω) increases.

For the stepped PDS operating with just air (LVF = 0%), Fig. 15 reveals a very small Ima(H), indicating very little damping. For journal speed equal to 3000 and 5250 rpm, the Ima(H) is negative. These are unusual results, as PDSs are known to produce significant positive direct damping. These results may be due to the characterization of the test rig damping. The equations of motion for the mechanical system described in Eq. (6) assume the test rig damping can be modeled as viscous damping, in which a dissipative force produced by the test rig is proportional to the velocity of the seal stator. In reality, the test rig damping may comprise of other types of damping, including structural damping and frictional damping. This may cause an overestimation of the structure contribution to the complex dynamic stiffness H_{ij}, creating negative results when extracting the test seal force coefficients.
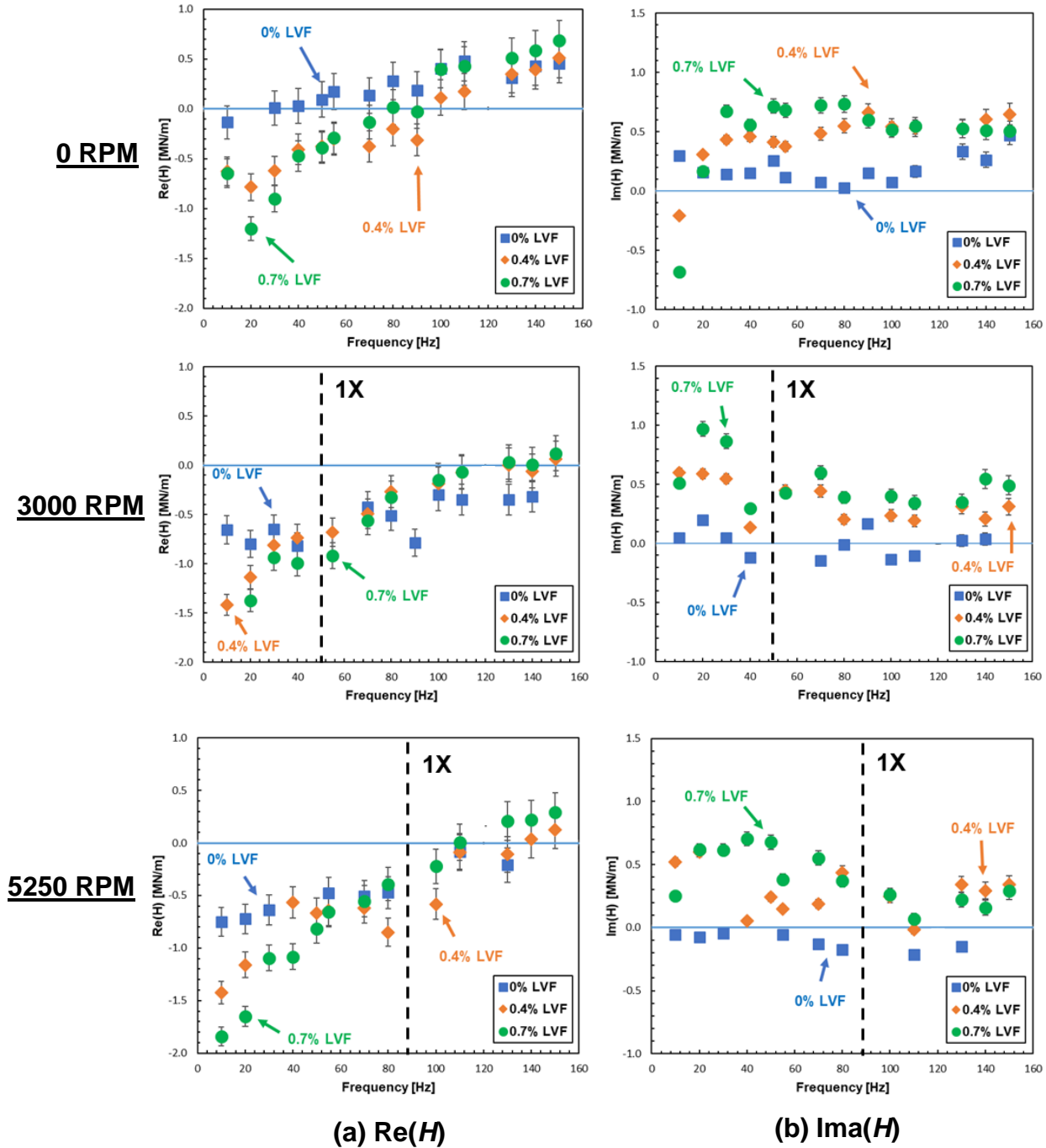
Fig. 15. Real and Imaginary Parts of Direct Dynamic Stiffness (*H*) for a Stepped PDS Operating with *P_s/P_e* = 2.5, LVF = (0, 0.4, 0.7)% ± 0.05%. Journal Speed = 0, 3000, & 5250 rpm.

Figure 16 presents the cross-coupled dynamic stiffness (*h*) and the effective damping coefficient (*C_{eff}*) for the stepped PDS with LVF = 0%, 0.4%, and 0.7%, *P_s/P_e* = 2.5, and journal speed = 0, 3000, and 5250 rpm. Similar to the results in Fig. 14, the measured cross-coupled effects are very small, thus the dominant factor contributing to the effective damping is the direct damping

coefficient. For operation with LVF = 0% (pure gas), C_{eff} of the stepped PDS is less than zero for journal speed = 3000 and 5250 rpm. As the liquid content increases, C_{eff} increases significantly, particularly at low excitation frequencies.

Stepped PDS, $P_S/P_e = 2.5$

(a) Re(h)

(b) C_{eff}
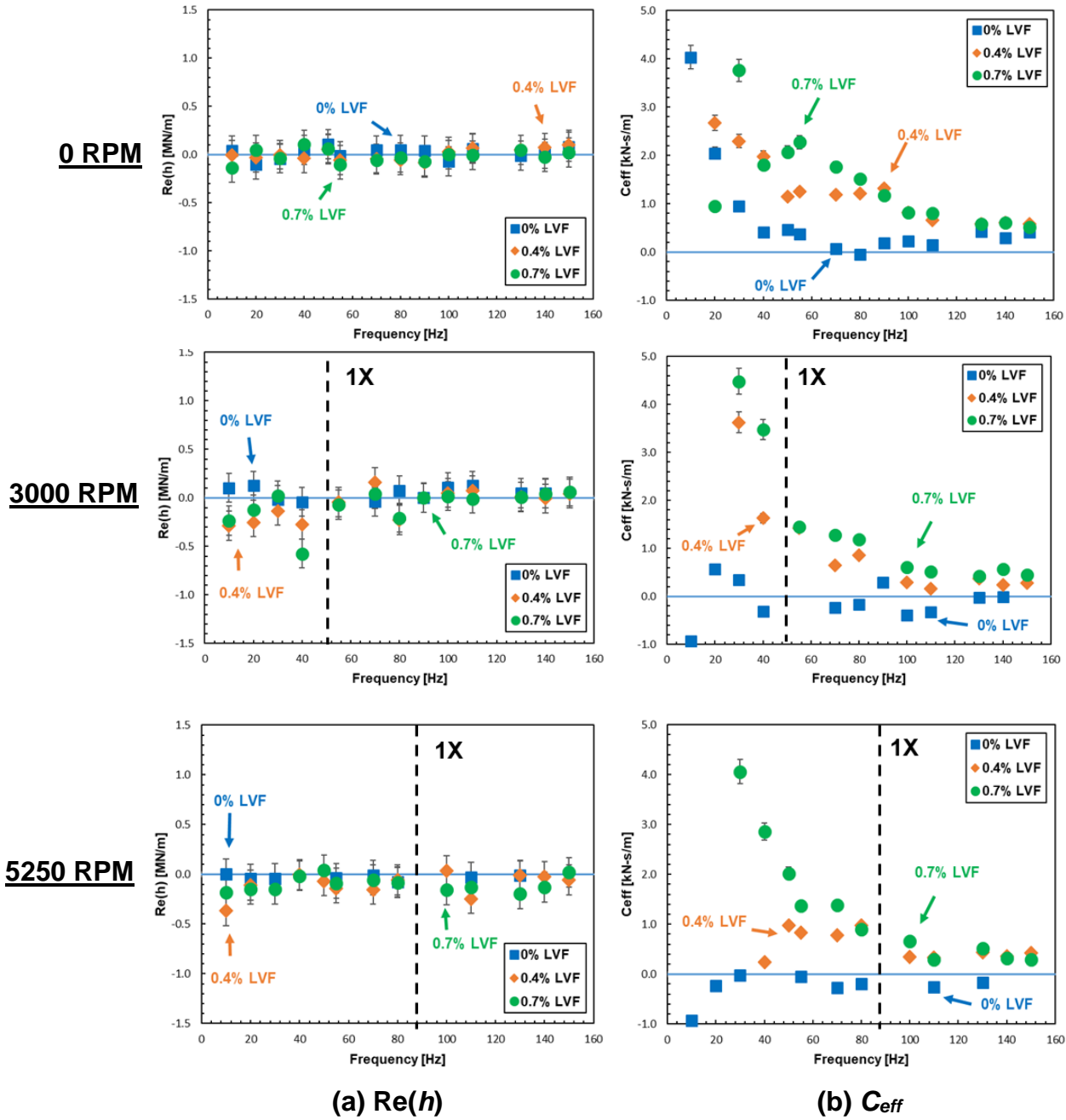
Fig. 16. Real Part of Cross-Coupled Dynamic Stiffness (h) and Effective Damping Coefficient (C_{eff}) for a Stepped PDS Operating with $P_S/P_e = 2.5$, LVF = (0, 0.4, 0.7)% ± 0.05%. Journal Speed = 0, 3000, & 5250 rpm.

Observed Seal Housing Subsynchronous Vibrations

Recall Vannini et al. [3] document the presence of an unexpected SSV during operation of a wet gas LS with a LVF ranging from 0% to 3%. The authors report the SSV occurring at 0.45X shaft speed with an amplitude of vibration of nearly twice that of the shaft speed motion.

For the current research, Fig. 17 presents a surface plot illustrating the amplitude of vibration at frequencies ranging from 0 to 3X shaft speed when operating the stepped LS over an elapsed time of 60 seconds. The journal speed = 3000 rpm (50 Hz) and P_s/P_e = 2.5. During 60 seconds, the LVF slowly decreases from 2.7% to 1.3%. Figure 17 shows very little SSVs, with only a low amplitude ($\approx$ 1.2 μm) vibration occurring at 0.5X shaft speed.
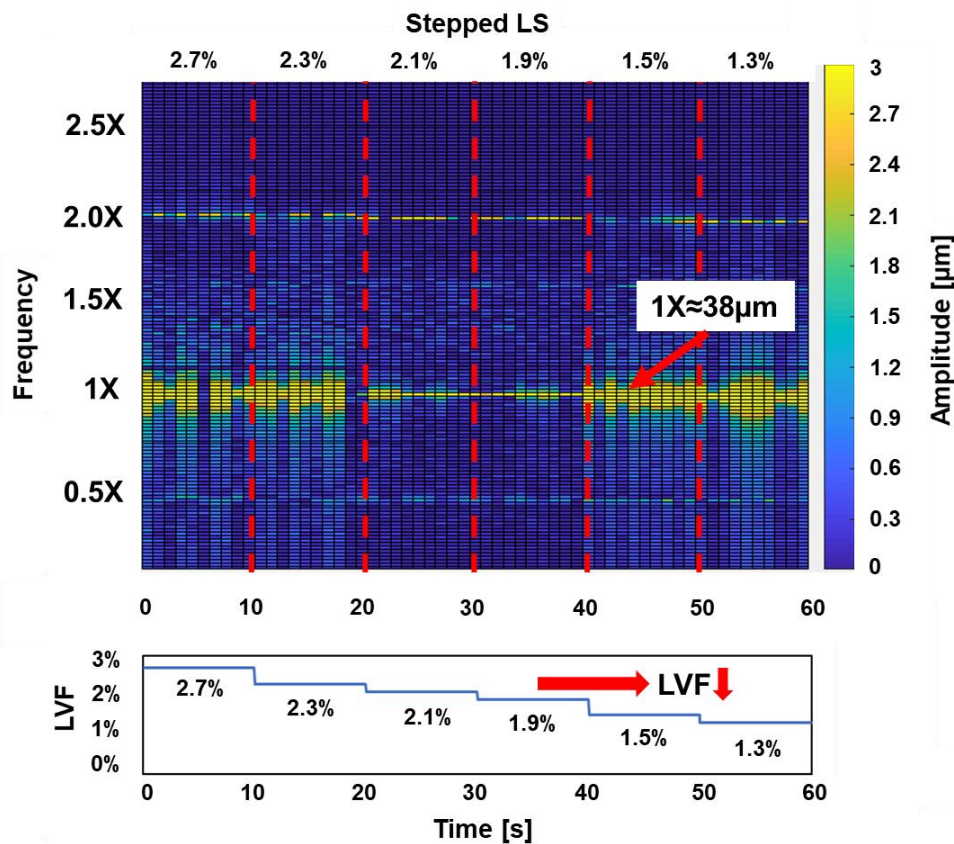
Fig. 17. SSV Amplitude of a Stepped LS Operating with Journal Speed = 3000 RPM, P_s/P_e = 2.5, and LVF Varying From 2.7% to 1.3%.

Figure 18 presents a surface plot illustrating the results of a similar experiment conducted with the stepped PDS. The journal speed is set to 3000 rpm and P_s/P_e = 2.5 to replicate the operating conditions for the stepped LS. During the elapsed time of 60 seconds, the LVF decreases slowly from 2.5% to 0.1%. Figure 18 reveals an unexpected broadband excitation occurring at subsynchronous frequencies (<50 Hz). The amplitude of the broadband excitation changes with

34

the liquid content. As the LVF decreases (more air is added to the mixture), the SSV amplitude decreases. A peak amplitude of 5 µm is recorded when LVF = 2.5%. Although this peak amplitude is small in comparison to the synchronous vibration amplitude of 38 µm, it is interesting to note that the SSV occurs only when operating the stepped PDS.

San Andrés and Lu [21] report a similar self-excited SSV occurring for a smooth annular seal operating with a two-phase flow. The authors report a broadband excitation happening when the GVF is greater than 20% (LVF < 80%). Contrary to the present results, the authors show an increase in amplitude and broadband frequency content as the GVF increases (liquid content decreases), although operation with pure air causes the excitation to suddenly disappear. The authors argue the self-excited SSVs are related to the sound speed of the mixture being too low, thus producing an acoustic resonance [21].
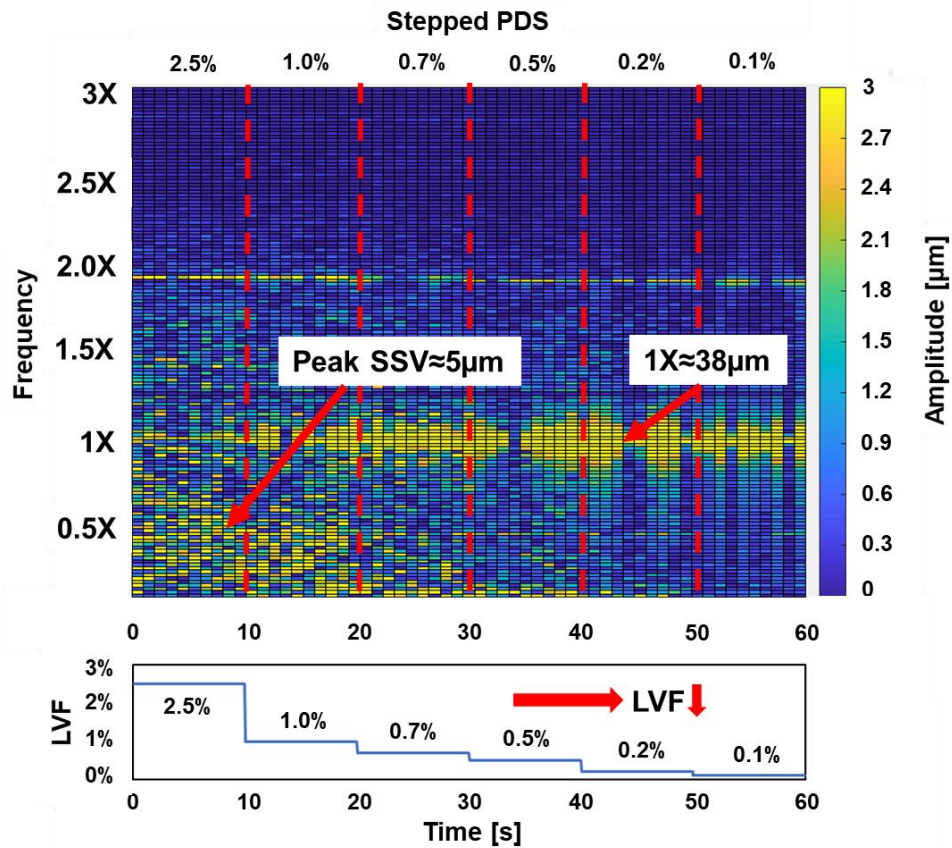
Fig. 18. SSV Amplitude of a Stepped PDS Operating with Journal Speed = 3000 RPM, P_s/P_e = 2.5, and LVF Varying From 2.5% to 0.1%.

Conclusions

This report details the leakage and force coefficients of a stepped PDS and a stepped LS operating with a two-phase flow. The stepped PDS and stepped LS feature the same rotor diameter, seal length, and number of blades, albeit differing slightly in radial clearance due to a manufacturing error. A dedicated two-phase flow test rig serves to measure the leakage of both seals operating under similar LVF and supply pressure. A parameter identification method produces force coefficients for both seals for excitation frequencies ranging from 0 to 150 Hz and operating with supply pressure of 2.5 bar(a) and journal speed up to 5250 rpm (88 Hz). The major findings are:

(a) A direct comparison of the measured leakages for both the stepped PDS and the stepped LS operating with pure gas shows the PDS has a lower loss coefficient (C_d). C_d quantifies the effectiveness of a seal in reducing leakage; a low C_d (< 1) indicates a more effective seal. As the LVF increases, the C_d of the stepped PDS decreases, due to the rapid increase in mixture density. Conversely, as LVF increases, the C_d of the stepped LS increases. For the stepped PDS operating with just air, $C_{d,PDS} = 0.23$; whereas for the stepped LS, $C_{d,LS} = 0.33$.

(b) The stepped PDS produces a larger Ima(H) (corresponding to the direct damping coefficient) than the stepped LS for all excitation frequencies when operating with the same LVF and supply pressure. The stepped PDS produces a larger Re(H) (corresponding to the direct stiffness coefficient) than the stepped LS for frequencies above 60 Hz and a smaller direct stiffness for frequencies below 60 Hz. The cross-coupled effects for both seals are too small for accurate measurement.

(c) The Ima(H) for the stepped PDS operating with a two-phase flow is positive and has a higher magnitude than the Ima(H) for a pure gas condition for all excitation frequencies. The Ima(H) for the stepped PDS operating with just air and journal speeds of 3000 and 5250 rpm is negative, a peculiar result likely due to the characterization of the test rig structure damping as viscous. At low frequencies (<60 Hz), the Re(H) for the stepped PDS decreases as the liquid content increases. At higher frequencies (>60 Hz), the Re(H) for the stepped PDS increases slightly as the liquid content increases.

(d) The stepped PDS produces unexpected broadband SSVs that increase in amplitude as the LVF increases. The SSVs are absent in tests with the stepped LS. The amplitude of the SSVs are small (≈ 5 µm) compared to the synchronous vibration amplitude (≈ 38 µm).

Comparisons of the current experimental results, namely leakage and dynamic force coefficients, vs. predictions (CFD and bulk flow models) are currently in progress.

References

[1] Childs, D.W., and Vance, J. M., 1997, "Annular Gas Seals and Rotordynamics of Compressors and Turbines," Proc. of the 26th Turbomachinery Symposium, Houston, TX, September 16-18, pp. 201-220. https://doi.org/10.21423/R1HT06.

[2] Vance, J. M,, and Schultz, R. R., 1993, "A New Damper Seal for Turbomachinery," Proc. of the 14th Biennial Conference on Mechanical Vibration and Noise, Albuquerque, NM, September 19-22, pp 139-148. https://doi.org/10.1115/DETC1993-0188.

[3] Vannini, G, Bertoneri, M., Del Vescovo, G., and Wilcox, M., 2014, "Centrifugal Compressor Rotordynamics in Wet Gas Conditions," Proc. of the 43rd Turbomachinery Symposium, Houston, TX, September 22-25, pp. 201-220. https://doi.org/10.21423/R1F93J.

[4] Vance, J.M., and Li, J., 1996, "Test Results of a New Damper Seal in Vibration Reduction in Turbomachinery," ASME J. Eng. Gas Turbines Power, **118**(10), pp. 843-846.

[5] Richards, R. L., Vance, J. M., Paquette, D. J., and Zeidan, F. Y., 1995, "Using A Damper Seal to Eliminate Subsynchronous Vibrations in Three Back-to-Back Compressors," Proc. of the 24th Turbomachinery Symposium, Houston, TX, September 26-28, pp. 59-71. https://doi.org/10.21423/R1MD4H.

[6] Ransom, D., Li, J., San Andrés, L., and Vance, J. M., 1999, "Experimental Force Coefficients for a Two-Bladed Labyrinth Seal and a Four-Pocket Damper Seal," ASME J. Tribol., **121**(4), pp. 370-376.

[7] Li, J., and San Andrés, L., 1999, "A Bulk-Flow Analysis of Multiple-Pocket Gas Damper Seals," ASME J. Eng. Gas Turbines Power, **121**(1), pp. 355-363.

[8] Li, J., Aguilar, R., San Andrés, L., and Vance, J. M, 2000, "Dynamic Force Coefficients of a Multiple-Blade, Multiple-Pocket Gas Damper Seal: Test Results and Predictions," ASME J. Tribol., **122**(1), pp. 317-322.

[9] Li, J., Kushner, F., and DeChoudhury, P., 2000, "Gas Damper Seal Test Results, Theoretical Correlation, and Applications in Design of High-Pressure Compressors," Proc. of the 29th Turbomachinery Symposium, Houston, TX, September 18-21, pp. 55-64. https://doi.org/10.21423/R1BH29.

[10] Li, J., Kushner, F., and DeChoudhury, P., 2002, "Experimental Evaluation of Slotted Pocket Damper Seals on a Rotating Test Rig," ASME Paper GT2002-30634.

[11] Ertas, B.H., and Vance, J.M., 2007, "Rotordynamic Force Coefficients for a New Damper Seal Design," ASME J. Tribol., **129**(1), pp. 365-374.

[12] Sheng, N, Ruggiero, E. J., Devi, R., Guo, J., and Cirri, M., 2011 "Experimental and Analytical Leakage Characterization of Annular Gas Seals: Honeycomb, Labyrinth and Pocket Damper Seals." ASME Paper GT2011-45217.

[13] Vannini, G., Bertoneri, M., Nielsen, K. K, Ludiciani, P., and Stronach, R., 2016, "Experimental Results and Computational Fluid Dynamics Simulations of Labyrinth and Pocket Damper Seals for Wet Gas Compression," ASME J. Eng. Gas Turbines Power, **138**(5), pp. 052501.

[14] San Andrés, L., Yang, J., and Lu, X., 2019, "On the Leakage, Torque, and Dynamic Force Coefficients of Air in Oil (Wet) Annular Seal: A Computational Fluid Dynamics Analysis Anchored to Test Data," ASME J. Eng. Gas Turbines Power, **140**(2), pp. 021008.

[15] Delgado, A., Thiele, J., Cangioli, F., San Andrés, L., and Yang, J., 2020, "Rotordynamic Performance of a Fully-Partitioned Damper Seal: Experimental and Numerical Results," Proc. of the 49th Turbomachinery Symposium, Houston, TX, December 8-10, pp. 1-29.

[16] Cangioli, F., Vannini, G., and Chirathadam, T., 2020, "A Novel Bulk-Flow Model for Pocket Damper Seals," ASME J. Eng. Gas Turbines Power, **142**(1), pp. 011012

[17] Vannini, G., Cioncolini, S., Del Vescovo, G., and Rovini, M., 2014, "Labyrinth Seal and Pocket Damper Seal High Pressure Rotordynamic Test Data," ASME J. Eng. Gas Turbines Power, **136**(2), pp. 022501.

[18] Yang, J., and San Andrés, L., 2021, "An Analytical Two-Phase Flow Model for Prediction of Leakage in Wet Gas Labyrinth Seals and Pocket Damper Seals. Is Simplicity Still Desired?" ASME Paper GT2021-58958.

[19] Yang, J., San Andrés, L., Lu, X., 2021, "On the Leakage and Dynamic Force Coefficients of a Novel Stepped Shaft Pocket Damper Seal: Experimental and Numerical Verification," ASME J. Eng. Gas Turbines Power, **143**(3), pp. 031002.

[20] San Andrés, L., Lu, X., and Liu, Q., 2016, "Measurements of Flow Rate and Force Coefficients in a Short-Length Annular Seal Supplied with a Liquid/Gas Mixture (Stationary Journal)," Tribol. Trans., **59**(4), pp. 758-767.

[21] San Andrés, L., and Lu, X., 2018, "Leakage, Drag Power and Rotordynamic Force Coefficients of an Air in Oil (Wet) Annular Seal," ASME J. Eng. Gas Turbines Power, **140**(1), pp. 012505.

[22] Lu, X., and San Andrés, L., 2019, "Leakage and Rotordynamic Force Coefficients of a Three-Wave (Air in Oil) Wet Annular Seal: Measurements and Predictions," ASME J. Eng. Gas Turbines Power, **141**(3), pp. 032503.

[23] San Andrés, L., 2009, *Modern Lubrication Theory,* "Experimental Identification of Bearing Force Coefficients," Notes 14, Texas A&M University Digital Libraries, [Mar 30, 2020], http://oaktrust.library.tamu.edu/handle/1969.1/93254, [April, 2021].

[24] San Andrés, L., Wu, T., Barajas-Rivera, J., Zhang, J., and Kawashita, R., 2019, "Leakage and Cavity Pressures in an Interlocking Labyrinth Gas Seal: Measurements Versus Predictions," ASME J. Eng. Gas Turbines Power, **141**(10), pp 101007.

Appendix A. Estimation of the Test Rig (Dry) Structure Force Coefficients

The dynamic force coefficients of the structure (system without flow of air and oil mixture) are found by utilizing the logarithmic decrement (log-dec) method, a common technique that uses measurements of the system free response to an impact load. Knowing the mass of the dry, unlubricated structure allows for the identification of the structure stiffness and damping coefficients.

The log-dec (δ) of a system free response is calculated by taking the natural logarithm of two separate peaks in the resulting data:

$$\delta = \frac{1}{n} \ln \left[\frac{X_1}{X_{1+n}} \right] \tag{A1}$$

where n represents the number of periods of motion that have passed between the two considered peaks. The exponential decay of the system response depends on the amount of damping within the system. Thus, the logarithmic decrement provides a method for calculating the system damping ratio (ζ):

$$\delta = \frac{2\pi\zeta}{\sqrt{1-\zeta^2}} \tag{A2}$$

The undamped natural frequency (ω_n) is extracted the damped natural frequency (ω_d) and damping ratio (ζ) since:

$$\omega_n = \frac{\omega_d}{\sqrt{1-\zeta^2}} \tag{A3}$$

The undamped natural frequency (ω_n) is a function of the system equivalent stiffness (K_e) and mass (M_e):

$$\omega_n = \sqrt{\frac{K_e}{M_e}} \tag{A4}$$

Figure A1 presents a sample free response of the two-phase flow test rig when subjected to an impact by a hammer. One can see that the system oscillates several times prior to returning to its equilibrium state. Figure A1 illustrates two peaks separated by $n = 4$ periods of motion.
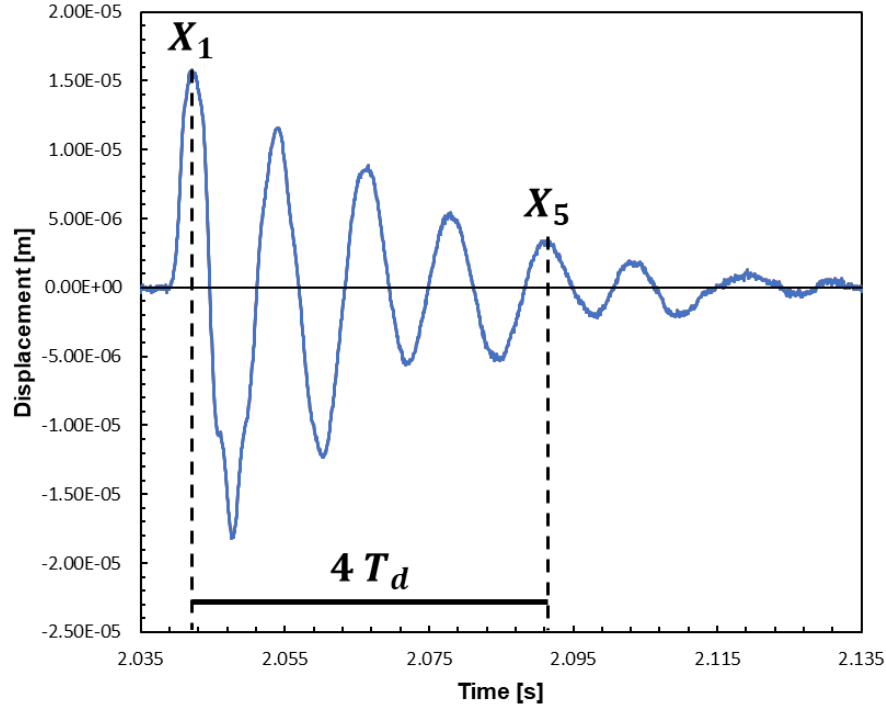
Fig. A1. Sample Free Response of Two-Phase Flow Test Rig When Subjected to Impact by Hammer, Illustrating Two Peaks Separated by 4 Periods of Motion.

Using Eq. (A1) and the amplitudes of displacement at these two peaks provides the log-dec value for the system. Thus, by using Eq. (A2), the system damping ratio is estimated from the resulting data. The damped natural frequency follows from the period of motion (T_d),

$$\omega_d = \frac{2\pi}{T_d} \tag{A5}$$

With the damped natural frequency and the damping ratio known, the undamped natural frequency is readily calculated using Eq. (A3). Given that the mass of the structure (M_{sc}) is known from the design of the test rig, the structure equivalent stiffness (K_h) is then found by using Eq. (A4). The structure equivalent damping (C_h) is then found from:

$$C_h = 2\xi \sqrt{K_h M_{sc}} \tag{A6}$$

A more reliable way to obtain the logarithmic decrement comes from applying a best linear fit to the following relationship and obtaining the slope:

$$\ln(X_{1+n}) = A - n\,\delta \tag{A7}$$

42

where $A = \ln(X_1)$ represents the natural logarithm of the first peak. Table details the force coefficients of the dry test rig. Note that the damping ratio (ζ) is rather large for a dry steel structure.

Table. A1. Structure Force Coefficients Identified Using Logarithmic Decrement Method.

K_h	3.77 ± 0.19 MN/m
M_{sc}	14 ± 0.1 kg
C_h	0.97 ± 0.05 kN-s/m
ζ	0.067
ω_n	82.55 Hz

References

[A1] San Andrés, L., 2008, *Mechanical Vibrations*, "MEEN 617 Notes, Handout 2a: Dynamic Response of Second Order Mechanical Systems with Viscous Dissipation Forces," Texas A&M University, https://rotorlab.tamu.edu/me617/handout2a_2008.pdf [March 16th, 2021].

Appendix B. Uncertainty for the Experimental Force Coefficients[1]

The total uncertainty related to the identification of dynamic stiffness and damping coefficients consists of a bias uncertainty and uncertainty due to variability. Bias uncertainty consists of inaccuracies resulting from a combination of the sensor resolution and precision of the data acquisition system. Uncertainty due to variability addressed the repeatability of the experimental results.

Bias Uncertainty

The bias uncertainty of each sensor depends on the resolution of the data acquisition system. For these experiments, a NI cDAQ-9174 chassis and a NI 9205 input module was used to record data. The resolution of the NI 9205 is 16 bits with an overall permissible input voltage range of ± 10 V. Therefore, the highest voltage resolution (R) of the NI 9205 input board is $20 \text{ V}/2^{16} = 0.31$ mV. In order to calculate the bias uncertainty of each sensor used, the resolution is divided by the sensitivity of the given sensor (b):

$$B_{sensor} = \frac{R}{b} \tag{B1}$$

The eddy current displacement sensors have a sensitivity of 207.7 mV/mil and 204.4 mV/mil in the X and Y directions respectively. Equation B1 shows the bias uncertainty for the displacement probes to be about 0.0015 mil for both sensors. During experimentation, the electromagnetic shakers induced vibrations at an average displacement of 5% of clearance. From Table 1, the given seal clearance is 0.18 mm (7.1 mil), giving an average displacement of 0.36 mil. Using the average measured displacement, the bias uncertainty of the eddy current displacement sensors corresponds to about 0.4%.

The load cells each have a sensitivity of 11.241 mV/N. With a resolution of 0.31 mV, the bias uncertainty of the load cells found using Eq. (B1) is found to be approximately 0.027 N. During experimentation, the average load observed was approximately 31 N. The bias uncertainty of the load cells using the average recorded load therefore corresponds to about 0.1%.

---

[1]This section follows portions of the uncertainty analysis presented in Ref. [B1]

The piezoelectric accelerometers both have a sensitivity of 10.60 mV/(m/s^2). With a resolution of 0.31 mV, the bias uncertainty of the accelerometers is approximately 0.03 m/s^2. During experimentation, the average recorded acceleration corresponds to approximately 2.97 m/s^2. Using the average measured acceleration, the bias uncertainty of the accelerometers is approximately 1.0%.

Recall Eq. (11) presents the method for calculating the complex impedance, containing both the dynamic stiffness and damping of the system. The total bias uncertainty in calculating the complex impedance is comprised of contributions from the eddy current sensors, accelerometers, and load cells. San Andrés [B2] presents the propagation of uncertainty for an experimental result comprised of a set of variables:

$$B_{total} = \sqrt{(B_{Disp})^2 + (B_{Acc})^2 + (B_{Load})^2} \tag{B2}$$

Using Equation B2, the total bias uncertainty in the identification of the system complex dynamic stiffness is approximately 1.08% of the given value.

Uncertainty due to Variability

Variability uncertainty deals with the repeatability of experimental results. The following analysis will consider the case in which P_s = 2.5 bar, GVF = 100%, and Ω = 0 RPM, to provide a typical value of uncertainty due to variability for the identification of dynamic force coefficients. The experimental results for these operating conditions were repeated a total of three times.

The uncertainty due to variability related to the dynamic stiffness and effective damping is defined as [B3]:

$$\varnothing = t\frac{S}{\sqrt{N}} \tag{B3}$$

where t represents the Student's t-distribution value of 4.303 corresponding to a 95% confidence interval for a sample size of $N = 3$ [B3]. S is the standard deviation provided by [B3]:

$$S = \sqrt{\frac{1}{(N-1)}\sum_{i=1}^{N}(x_i - \bar{x})^2} \tag{B4}$$

where x_i denotes the standard deviation of the sample, $\bar{x}$ denotes the mean value of the sample, and N denotes the number of tests performed, three. Note that each test frequency analyzed for the given operating condition (fifteen frequencies ranging from 10 Hz to 150 Hz) provides one experimental result each for dynamic stiffness and damping. Thus, the results at this operating condition is comprised of fifteen independent results. The dynamic stiffness and damping variability uncertainties was taken to be the average among all test frequencies. The uncertainty due to variability for the case in which $P_S = 2.5$ bar(a), $GVF = 100\%$, and $\Omega = 0$ RPM is then calculated using the mean value among all test frequencies to provide the uncertainty in terms of a percentage:

$$V_{\text{Re}(H)} = \frac{\phi_{\text{Re}(H)}}{\text{Re}(H)} = 4.47\% \tag{B5}$$

$$V_{\text{Ima}(H)} = \frac{\phi_{\text{Ima}(H)}}{\text{Ima}(H)} = 5.75\% \tag{B6}$$

Total Uncertainty

The total uncertainty related to the identification of the dynamic force coefficients is a combination of the bias uncertainty and uncertainty due to variation. For the case with operating conditions $P_S = 2.5$ bar, $GVF = 100\%$, and $\Omega = 0$ RPM, the resulting total uncertainties are:

$$U_{\text{Re}(H)} = \sqrt{(B_{\text{Re}(H)})^2 + (V_{\text{Re}(H)})^2} = \sqrt{1.08^2 + 4.47^2} = 4.60\% \tag{B7}$$

$$U_{\text{Ima}(H)} = \sqrt{(B_{\text{Ima}(H)})^2 + (V_{\text{Ima}(H)})^2} = \sqrt{1.08^2 + 5.75^2} = 5.85\% \tag{B8}$$

References

[B1] San Andrés, L., Rodríguez, B., 2020, *"Experimental Force Coefficients in a Sealed Ends SFD Supplied with Lubricant Through a Check Valve"*, Technical Progress Report TRC-SFD-02-20, Turbomachinery Research Consortium (TRC).

[B2] San Andrés, L., 2019, *Measurements of Sounds and Vibration*, "Sensor calibration & uncertainty in measurements and engineering analysis," Texas A&M University, https://rotorlab.tamu.edu/me459/NOTES%205%20Sensors%20and%20Uncertainty%20Analysis.pdf [March 23rd, 2020].

[B3] Beckwith, T., Marangoni, R., and Lienhard., J., 1993, "Mechanical Measurements," Prentice Hall. 5th edition, pp. 82.

Appendix C. Uncertainty in Measurement of Flow Rate and Gas Volume Fraction

Two flow meters provide the measured volumetric flow rate of oil and air required to calculate the total leakage and gas volume fraction. Data was gathered using digital displays, hence the NI cDAQ-9174 chassis and a NI 9205 input module were not used in recording leakage or gas volume fraction. The uncertainty in calculation of leakage and gas volume fraction is primarily due to the uncertainty of the sensors.

Uncertainty of Sensors/Transducers

The amount of leakage of the oil and air mixture experienced by the test seal under a given operating condition is estimated by summing the mass flow rate of oil and air. The mass flow rate of each is found by measuring the volumetric flow rate using a flow meter and multiplying by the known density. One can see that the total leakage of the test seal is a function of the air volumetric flow rate and the oil volumetric flow rate, and therefore has an uncertainty associated with the error in the two flow meters. Similarly, the gas volume fraction is also a function of the two volumetric flow rates, as given by Eq. (5). Therefore, estimations of gas volume fraction also have a degree of uncertainty related to the accuracy of the flow meters.

The accuracy for the oil flow meter over its linear range is published at $\pm$ 2.0% of reading [C1]. Similarly, the accuracy for the air flow meter over its linear range is published at $\pm$ 0.30 % of reading [C2]. The propagation of uncertainties when estimating seal leakage and gas volume fraction is given by Eq. (C1) [B2].

$$U_{Leakage,\ GVF} = \sqrt{U^2_{Oil\ Flow\ Meter} + U^2_{Air\ Flow\ Meter}} = \sqrt{(2.0\%)^2 + (0.3\%)^2} \cong 2.02\%$$

(C1)

Using Eq. (C1), the total uncertainty in estimation of seal leakage and gas volume fraction is approximately 2.02%.

References

[C1] "FTB790 Series Turbine Flowmeters," User's guide for FTB790 series turbine flowmeters, Omega.

[C2] "FT Series – Turbine Flowmeters for Gas Applications," Product data sheet for FT series turbine flowmeters, FTI Flow Technologies.